

¹ **Nucleotide inhibition of the**

² **pancreatic ATP-sensitive K⁺ channel**

³ **explored with patch-clamp**

⁴ **fluorometry**

⁵ **Samuel G. Usher¹, Frances M. Ashcroft^{1*}, Michael C. Puljung^{1*}**

*For correspondence:

frances.ashcroft@dpag.ox.ac.uk

⁶ Department of Physiology, Anatomy and Genetics, University of Oxford,
(FMA);

michael.puljung@dpag.ox.ac.uk

(MCP)

⁷ Oxford OX1 3PT, United Kingdom

⁸

⁹ **Abstract** Pancreatic ATP-sensitive K⁺ channels (K_{ATP}) comprise four inward rectifier
¹⁰ subunits (Kir6.2), each associated with a sulphonylurea receptor (SUR1). ATP/ADP
¹¹ binding to Kir6.2 shuts K_{ATP}. Mg-nucleotide binding to SUR1 stimulates K_{ATP}. In the
¹² absence of Mg²⁺, SUR1 increases the apparent affinity for nucleotide inhibition at Kir6.2
¹³ by an unknown mechanism. We simultaneously measured channel currents and
¹⁴ nucleotide binding to Kir6.2. Fits to combined data sets suggest that K_{ATP} closes with
¹⁵ only one nucleotide molecule bound. A Kir6.2 mutation (C166S) that increases channel
¹⁶ activity did not affect nucleotide binding, but greatly perturbed the ability of bound
¹⁷ nucleotide to inhibit K_{ATP}. Mutations at position K205 in SUR1 affected both nucleotide
¹⁸ affinity and the ability of bound nucleotide to inhibit K_{ATP}. This suggests a dual role for
¹⁹ SUR1 in K_{ATP} inhibition, both in directly contributing to nucleotide binding and in
²⁰ stabilising the nucleotide-bound closed state.

²¹

22 Introduction

23 ATP-sensitive K⁺ channels (K_{ATP}) couple the metabolic state of a cell to its electrical ac-
 24 tivity (*Ashcroft and Rorsman, 2013*). In pancreatic β-cells, closure of K_{ATP} in response to
 25 glucose uptake triggers insulin secretion. As such, mutations in K_{ATP} that affect its re-
 26 sponse to changes in cellular metabolism cause diseases of insulin secretion, e.g. neona-
 27 tal diabetes and persistent hyperinsulinemic hypoglycaemia of infancy (PHHI; *Quan et al.*
 28 (*2011*); *Ashcroft et al. (2017)*). K_{ATP} is composed of four inwardly rectifying K⁺ channel
 29 subunits (Kir6.2 in pancreatic β-cells), which form the channel pore and four modula-
 30 tory sulphonylurea receptor subunits (SUR1 in β-cells; Figure 1A; *Aguilar-Bryan et al.*
 31 (*1995*); *Inagaki et al. (1995)*; *Sakura et al. (1995)*; *Inagaki et al. (1997)*). SUR1 is a mem-
 32 ber of the ABC transporter family but lacks any transport activity (*Aguilar-Bryan et al.*,
 33 *1995*; *Tusnady et al., 1997*). K_{ATP} responds to metabolism via adenine nucleotide binding
 34 to three distinct classes of intracellular nucleotide-binding site (one on each Kir6.2 sub-
 35 unit and two on each SUR1 subunit—making twelve sites in total (*Vedovato et al., 2015*).
 36 Binding of ATP or ADP to Kir6.2 inhibits K_{ATP} channel activity (*Tucker et al., 1997*; *Proks*
 37 *et al., 2010*), whereas binding of nucleotides to SUR1 stimulates K_{ATP} (*Nichols et al., 1996*;
 38 *Tucker et al., 1997*). The stimulatory activity of nucleotides on K_{ATP} depends on Mg²⁺
 39 (*Gribble et al., 1998*), whereas their inhibitory effect on Kir6.2 does not (*Tucker et al.*,
 40 *1997*).

41 In addition to nucleotide-dependent activation, SUR1 confers several other properties
 42 on the Kir6.2. First, association with SUR1 increases the open probability (P_{open}) of Kir6.2
 43 (*Babenko and Bryan, 2003*; *Chan et al., 2003*; *Fang et al., 2006*). Despite this increase in
 44 P_{open} , SUR1 also paradoxically increases the apparent affinity for nucleotide inhibition at
 45 Kir6.2 by an unknown mechanism (*Tucker et al., 1997*). SUR1 is also responsible for high-
 46 affinity inhibition of K_{ATP} by antidiabetic sulphonylureas and glinides as well as activation
 47 by K_{ATP} -specific K⁺ channel openers (*Tucker et al., 1997*). Finally, SUR1 and Kir6.2 must co-
 48 assemble to ensure mutual exit from the endoplasmic reticulum and correct trafficking

⁴⁹ to the plasma membrane (*Zerangue et al., 1999*).

⁵⁰ To date, the primary means of studying nucleotide-dependent effects on K_{ATP} chan-
⁵¹ nel function has been with electrophysiological approaches, which measure the summed
⁵² activity of all three classes of binding site acting in concert. Thus, it can be difficult to sep-
⁵³ arate the contributions of each class of site to the opening and closing of the channel
⁵⁴ pore and to properly distinguish between nucleotide binding and channel gating. To
⁵⁵ overcome these limitations, we have applied a novel approach to directly measure nu-
⁵⁶ cleotide binding to each individual class of site in K_{ATP} (*Puljung et al., 2019*). This method
⁵⁷ utilizes Förster resonance energy transfer (FRET) between channels labelled with the flu-
⁵⁸ orescent unnatural amino acid 3-(6-acetylnaphthalen-2-ylamino)-2-aminopropanoic acid
⁵⁹ (ANAP) and fluorescent trinitrophenyl (TNP) analogues of adenine nucleotides (Figure 1B).
⁶⁰ As we show here, this method is readily combined with patch-clamp electrophysiology so
⁶¹ that nucleotide binding and regulation of current can be measured simultaneously. This
⁶² has enabled us to quantitatively assess nucleotide binding to Kir6.2 and explore how this
⁶³ is coupled to channel inhibition in both wild-type K_{ATP} and K_{ATP} carrying mutations that
⁶⁴ impair ATP inhibition.

⁶⁵ Results

⁶⁶ **Measuring nucleotide binding to Kir6.2.** We previously used this FRET-based bind-
⁶⁷ ing assay to measure nucleotide binding to the second nucleotide-binding site of SUR1
⁶⁸ (*Puljung et al., 2019*). To measure binding to Kir6.2 in the complete K_{ATP} complex (four
⁶⁹ full-length Kir6.2 subunits co-expressed with four full-length SUR1 subunits), we replaced
⁷⁰ a tryptophan at position 311 (W311) that is 26 Å from the location of the inhibitory nucleotide-
⁷¹ binding site on Kir6.2 with ANAP (Figure 1C) such that each subunit is labelled with one
⁷² ANAP molecule. We designate this construct Kir6.2*. Based on the theoretical FRET ef-
⁷³ ficiency calculated from the Förster equation and available cryo-EM structures (*Martin*
⁷⁴ *et al., 2017, 2019*), we expect 91% FRET efficiency between ANAP at position 311 and a
⁷⁵ TNP-ATP molecule bound to Kir6.2, and only 4% FRET efficiency to TNP-ATP bound to the

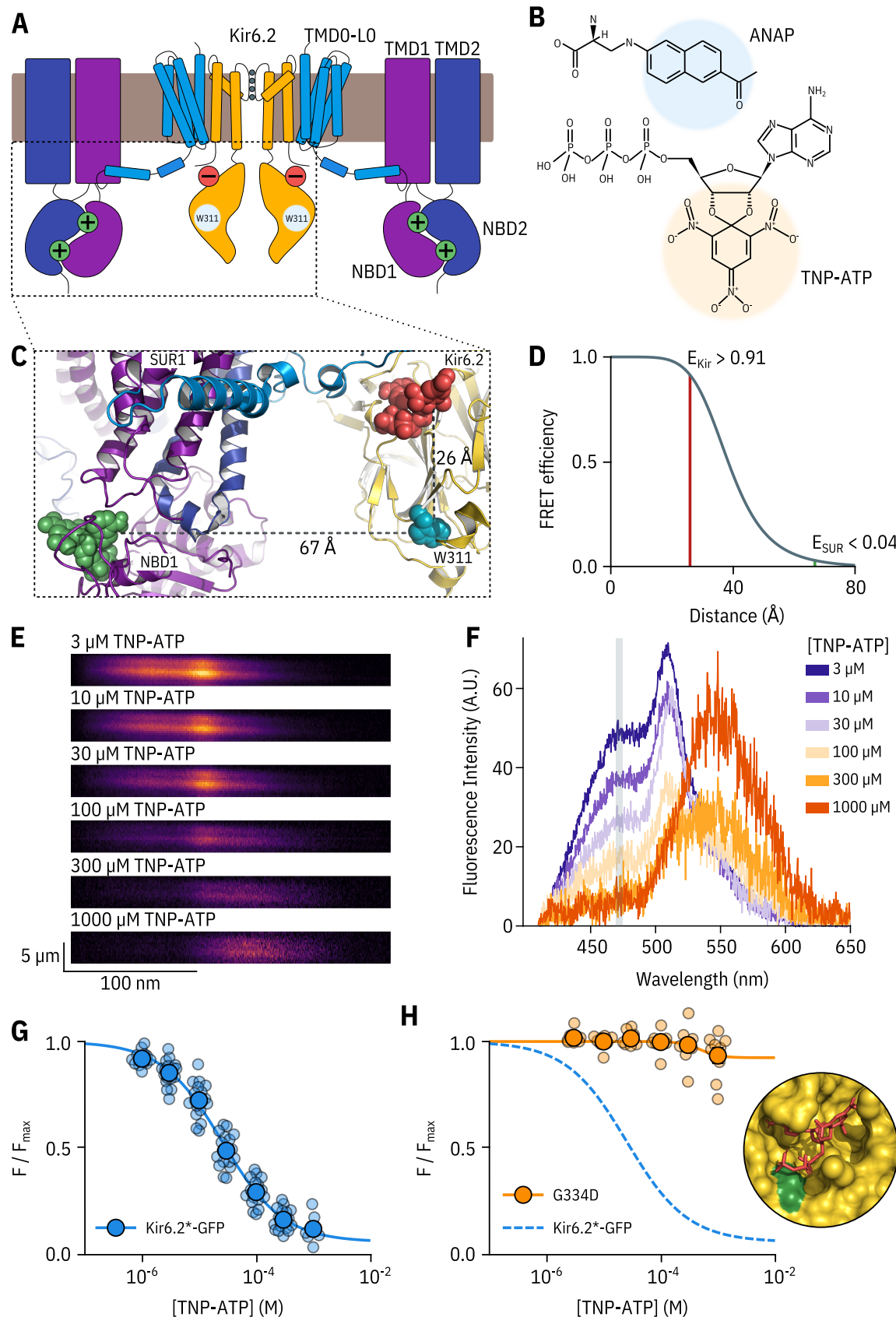


Figure 1. A FRET assay to measure nucleotide binding to Kir6.2.

Figure 1. A FRET assay to measure nucleotide binding to Kir6.2. **A.** Cartoon illustrating the topology of K_{ATP}. The inhibitory nucleotide-binding site on Kir6.2 is shown in red; the stimulatory nucleotide-binding sites on SUR1 are shown in green. The three transmembrane domains of SUR1 are designated TMD0, TMD1, and TMD2. The loop connecting TMD0 to TMD1 is designated L0. The nucleotide binding domains of SUR1 are labelled NBD1 and NBD2. **B.** Chemical structures of ANAP and TNP-ATP. The fluorescent moieties are highlighted. **C.** Side view of the structure of the cytosolic domains of Kir6.2 (PDB accession #6BAA) and one SUR1 subunit (PDB accession #6PZI). TNP-ATP (red, from PDB accession #5XW6) was docked into the nucleotide-binding site of Kir6.2 and positioned in NBS1 of SUR1 (green, from PDB accession #3AR7) by alignment as described in Materials and Methods. Distances from the centre of mass of the six-membered ring of the native tryptophan at position 311 in Kir6.2 to the centre of mass of the trinitrophenyl moieties of the TNP-ATPs are displayed in Å. **D.** Theoretical FRET efficiency between ANAP and TNP-ATP as a function of distance, calculated from the Förster equation. The distances and corresponding FRET efficiencies between ANAP at position 311 and TNP-ATP bound to Kir6.2 (E_{Kir}) and SUR1 (E_{SUR}) are indicated. Our calculated R₀ (the distance at which FRET efficiency is half maximal) for ANAP and TNP-ATP is 38.4 Å. **E.** Spectral images acquired from an unroofed membrane expressing Kir6.2*-GFP + SUR1 and exposed to increasing concentrations of TNP-ATP. The y-dimension in each image represents distance. The x-dimension represents wavelength. **F.** Line-averaged, background-subtracted spectra from **E** displayed with increasing concentrations of TNP-ATP coloured from purple to orange. The three fluorophores have distinct peaks: ANAP at 472 nm, GFP at 508 nm, and TNP-ATP at 561 nm. The shaded rectangle indicates the wavelength range used to measure ANAP intensity. **G.** Concentration-response relationship for binding of TNP-ATP to Kir6.2*-GFP + SUR1 in unroofed membranes. Data were plotted as F/F_{max} , where F_{max} is the fluorescence intensity of ANAP in the absence of nucleotide. The smooth curve is a descriptive Hill fit. $EC_{50} = 25.6 \mu\text{M}$, $h = 0.82$, $E_{max} = 0.93$, $n = 18$. **H.** Concentration-response relationship for binding of TNP-ATP to Kir6.2*,G334D-GFP + SUR1 in unroofed membranes. The dashed blue curve is the fit from **G**. The orange curve is a descriptive Hill fit to the G334D data. $EC_{50} = 493 \mu\text{M}$, $h = 2.63$, $E_{max} = 0.08$, $n = 9$. The inset shows the location of G334D (green) in relation to the inhibitory ATP binding site on Kir6.2 (PDB accession #6BAA). TNP-ATP (PDB accession #5XW6) shown in red sticks.

Figure 1 – figure supplement 1. ANAP labelling is specific and only full-length Kir6.2 is expressed at the cell membrane.

Figure 1 – figure supplement 2. Kir6.2*-GFP is functionally similar to Kir6.2-GFP.

⁷⁶ closest nucleotide-binding site on SUR1 (nucleotide binding site 1, Figure 1D). We also ex-
⁷⁷ pect very little FRET between ANAP at position 311 and TNP-ATP bound to neighbouring
⁷⁸ Kir6.2 subunits (see Materials and Methods for more details on our calculations).

⁷⁹ ANAP incorporation into Kir6.2 was achieved as described previously (*Chatterjee et al.*,
⁸⁰ *2013; Zagotta et al., 2016; Puljung et al., 2019*). Briefly, HEK-293T cells were co-transfected
⁸¹ with a plasmid encoding a Kir6.2 construct with a C-terminal GFP tag and an amber stop
⁸² codon (TAG) replacing the codon corresponding to amino acid position 311 (W311^{TAG}-
⁸³ GFP) and a plasmid encoding an ANAP-specific tRNA/tRNA synthetase pair (pANAP). We
⁸⁴ also included a dominant negative eukaryotic ribosomal release factor (eRF-E55D) in
⁸⁵ our transfections, which has been shown to increase the amount of full-length, ANAP-
⁸⁶ labelled protein (*Schmied et al., 2014; Puljung et al., 2019*). When cultured in the pres-
⁸⁷ ence of ANAP, full length, fully ANAP-labelled Kir6.2 protein was produced and success-
⁸⁸ fully trafficked to the membrane in the presence of SUR1 (Figure 1—Figure supplement
⁸⁹ 1; see Materials and Methods). We used GFP-tagged Kir6.2 constructs throughout this
⁹⁰ study unless otherwise indicated, to help identify cells or membranes expressing K_{ATP}.

⁹¹ In all our experiments, we measured currents in excised patches from cells express-
⁹² ing K_{ATP} in the absence of Mg²⁺. Under such conditions, nucleotides can bind to both
⁹³ sites on SUR1, but no activation occurs, allowing inhibitory currents to be measured in
⁹⁴ isolation (*Gribble et al., 1998; Ueda et al., 1999; Puljung et al., 2019*). Kir6.2*-GFP + SUR1
⁹⁵ exhibited nearly identical sensitivity to ATP inhibition as Kir6.2-GFP + SUR1 (Figure 1—
⁹⁶ Figure supplement 2A), indicating that replacement of W311 with ANAP did not affect
⁹⁷ inhibition of K_{ATP}. Whereas both constructs were inhibited by TNP-ATP with a higher ap-
⁹⁸ parent affinity relative to ATP, incorporation of ANAP resulted in channels with a slightly
⁹⁹ lower TNP-ATP sensitivity relative to wild-type (IC_{50} of 6.2 μM compared to an IC_{50} of
¹⁰⁰ 1.2 μM, Figure 1—Figure supplement 2B,C).

¹⁰¹ Kir6.2-GFP has been demonstrated to traffic to the plasma membrane in the absence
¹⁰² of SUR1 and form functional channels (*John et al., 1998; Makhina and Nichols, 1998*). In
¹⁰³ a luminescence-based, surface-expression assay, we did not detect HA-tagged Kir6.2*-

104 GFP at the plasma membrane in the absence of SUR1 (Figure 1—Figure supplement 1E).
 105 To verify that the currents measured in our experiments in which Kir6.2*-GFP was co-
 106 transfected with SUR1 were the result of Kir6.2*-GFP + SUR1 and not Kir6.2*-GFP alone,
 107 we measured the sensitivity of currents to inhibition by the sulphonylurea tolbutamide,
 108 a property conferred by the SUR1 subunit. Whereas currents from unlabelled wild-type
 109 Kir6.2-GFP expressed in the absence of SUR1 were not affected by 100 μ M tolbutamide,
 110 both wild-type Kir6.2-GFP and Kir6.2*-GFP currents were inhibited to a similar extent
 111 by when expressed with SUR1 (46.5% \pm 0.04% and 57.7% \pm 0.02%, respectively; Figure
 112 1—Figure supplement 2D). The extent of inhibition was similar to previous measure-
 113 ments of tolbutamide inhibition (*Tucker et al., 1997*), confirming that Kir6.2*-GFP was
 114 co-assembled with SUR1 at the plasma membrane.

115 To measure nucleotide binding, cells transfected with Kir6.2*-GFP + SUR1 were briefly
 116 sonicated, leaving behind unroofed plasma membrane fragments (*Heuser, 2000; Zagotta*
 117 *et al., 2016; Puljung et al., 2019*) containing ANAP-labelled K_{ATP} channels with the intra-
 118 cellular nucleotide-binding sites exposed to the bath solution. The sample was excited
 119 with a 385 nm LED and emitted fluorescence from the membrane fragments was passed
 120 through a spectrometer, allowing us to separate ANAP, GFP, and TNP-ATP fluorescence
 121 by peak wavelength (Figure 1E,F). As expected from FRET, increasing the concentration of
 122 TNP-ATP caused a decrement in the ANAP peak at 472 nm and a concomitant increase in
 123 the TNP-ATP peak at 561 nm (Figure 1F). We used the quenching of the ANAP peak as a di-
 124 rect measure of TNP-ATP binding as this signal was specific to K_{ATP} . In contrast, the peak
 125 TNP-ATP fluorescence may include contributions from both specific and non-specific nu-
 126 cleotide binding, as well as direct excitation of TNP-ATP in solution by the 385 nm excita-
 127 tion light. Due to the sharp cut-off of the GFP emission spectrum at shorter wavelengths,
 128 our measurements of peak ANAP fluorescence were unaffected by the presence of the
 129 GFP tag on Kir6.2.

130 We fit concentration-response data for ANAP quenching by TNP-ATP with the Hill
 131 equation, to produce estimates of apparent affinity (EC_{50} , the half maximal effective con-

132 centration) and E_{max} (ANAP quenching at saturating concentrations of TNP-ATP; Figure
 133 1G). E_{max} was 93%, in good agreement with the 91% predicted by the Förster equation
 134 and theoretical distance measurements (Figure 1D), suggesting that we were able to mea-
 135 sure binding directly to the inhibitory site at Kir6.2. To confirm this, we introduced a well-
 136 studied neonatal diabetes mutation (G334D) into the Kir6.2 binding site, which drastically
 137 reduces the sensitivity of the channel to inhibition by nucleotides (*Drain et al., 1998; Ma-*
 138 *sia et al., 2007; Proks et al., 2010*). Based on the cryo-electron microscopy structures of
 139 K_{ATP} , this mutation is expected to interfere with nucleotide binding directly (Figure 1H
 140 inset, *Martin et al. (2017)*). The resulting construct Kir6.2*,G334D-GFP + SUR1 displayed
 141 drastically reduced ANAP quenching over the range of TNP-ATP concentrations tested.
 142 We therefore conclude that our binding measurements were specific for the inhibitory
 143 nucleotide-binding site on Kir6.2. This observation is consistent with the interpretation
 144 that the G334D mutation causes neonatal diabetes by preventing nucleotide binding.

145 **Measuring current inhibition and nucleotide binding simultaneously.** The ap-
 146 parent affinity of Kir6.2*-GFP + SUR1 for TNP-ATP in unroofed membranes was 25.6 μM
 147 (Figure 1G and Table 1). This value is higher than the apparent affinity for nucleotide inhi-
 148 bition (6.2 μM) measured using patch-clamp (Figure 1—Figure supplement 2C). However,
 149 both binding and current measurement are a function of the intrinsic binding affinity, the
 150 channel P_{open} , and the ability of agonist, once bound, to close the channel. Furthermore,
 151 the functional state of K_{ATP} in unroofed membranes is unclear. This is a particular prob-
 152 lem with K_{ATP} channels, which run down due to slow dissociation of phosphatidylinositol
 153 4,5-bisphosphate (PIP₂), reducing the P_{open} over time even in the absence of nucleotides
 154 (*Proks et al., 2016*).

155 As measuring either nucleotide binding or ionic currents in isolation only offers lim-
 156 ited mechanistic insight into inhibition of K_{ATP} , we turned to patch-clamp fluorometry
 157 (PCF, *Proks et al. (2016); Zheng and Zagotta (2003)*). Using PCF, we can measure TNP-ATP
 158 binding to Kir6.2 and channel activity simultaneously (Figure 2), providing us with direct
 159 access to the relationship between nucleotide binding and channel function. We simul-

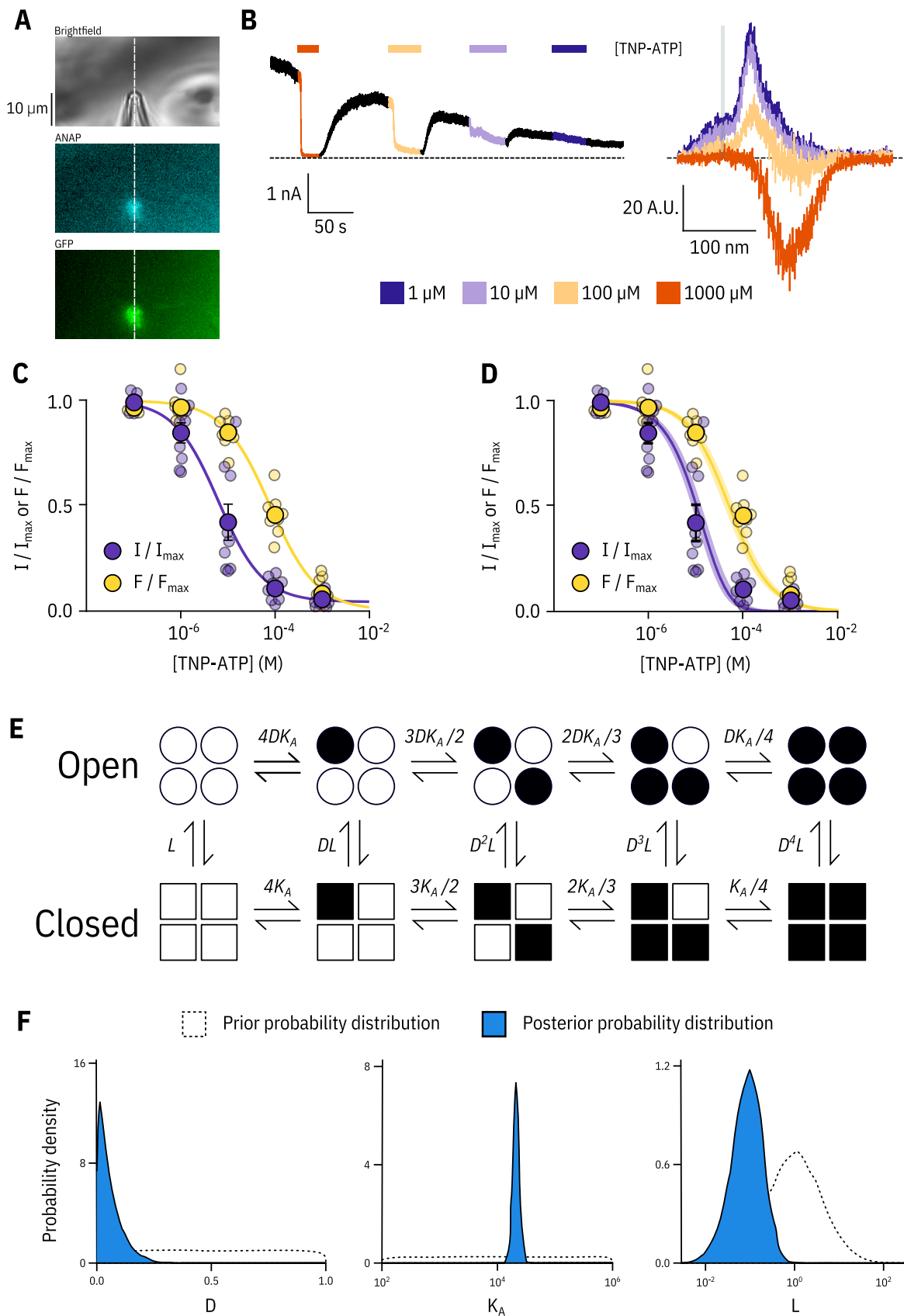


Figure 2. Simultaneous measurements of nucleotide binding and channel current.

Figure 2. Simultaneous measurements of nucleotide binding and channel current. **A.** Brightfield and fluorescence images of a patch pipette and excised, inside out patch expressing Kir6.2*-GFP + SUR1, with the location of the centre of the spectrometer slit overlaid as a white, vertical line. **B.** Current (left) and spectra (right) acquired from the same excised, inside-out patch exposed to TNP-ATP and coloured according to concentration. **C.** Concentration-response ($n = 9$) for TNP-ATP inhibition of Kir6.2*-GFP + SUR1 currents (I/I_{max}) and for quenching of ANAP fluorescence (F/F_{max}). Both current inhibition and fluorescence quenching were fit to the Hill equation. Current inhibition: $IC_{50} = 6.23 \mu\text{M}$, $h = 0.92$, $I_{max} = 0.96$, fluorescence quenching: $EC_{50} = 77.7 \mu\text{M}$, $h = 0.87$, $E_{max} = 1.00$. **D.** The same data as in **C** fit to an MWC-type model. Solid curves represent the median fit; shaded areas represent the 95% quantile interval. Values for the fits are reported in the text and in Table 3. **E.** MWC-type model for inhibition of K_{ATP} by nucleotides. Open subunits are shown as circles; closed are shown as squares. Nucleotide-bound subunits are represented by filled symbols. L , D , and K_A are defined in the text. **F.** Posterior probability distributions for the MWC-type model generated by MCMC fits to the data in **C** overlaid on the prior probability distribution (dashed line) for each parameter.

Figure 2 – figure supplement 1. Fixing L does not affect estimates of D and K_A .

Figure 2 – figure supplement 2. Model selection.

Figure 2 – figure supplement 3. Bleaching correction for PCF experiments.

¹⁶⁰ taneously measured fluorescence emission spectra and ionic currents for Kir6.2*-GFP +
¹⁶¹ SUR1 in inside-out, excised membrane patches. The apparent negative fluorescence in-
¹⁶² tensities at high TNP-ATP concentrations are due to imperfect background subtraction,
¹⁶³ and do not affect our measurements of ANAP intensities (see Materials and Methods). As
¹⁶⁴ before, all measurements were performed in the presence of Mg^{2+} chelators, such that
¹⁶⁵ nucleotide inhibition could be measured in the absence of activation (*Tucker et al., 1997*;
¹⁶⁶ *Gribble et al., 1998*). Strikingly, current inhibition occurred at a lower range of concen-
¹⁶⁷ trations compared to nucleotide binding (Figure 2C,D). The apparent IC_{50} for inhibition
¹⁶⁸ calculated from Hill fits was an order of magnitude lower than the EC_{50} for binding mea-
¹⁶⁹ sured in the same patches (Figure 2C, Table 2). We considered several different gating
¹⁷⁰ models to explain this observation. In each model, we assumed the channel pore was
¹⁷¹ able to open and close in the absence of ligand with an equilibrium constant L , where
¹⁷² $P_{open} = L/(L + 1)$ and $L > 0$, reflecting the ability of K_{ATP} to open and close in the ab-

sence of nucleotides. This excludes the possibility of induced-fit models which would not predict unliganded channel closings. Induced fit models also cannot account for separation between the binding and gating curves which we observe in Figure 2C,D (*Changeux and Edelstein, 2011*). Each model also had parameters representing the intrinsic binding affinity to the closed state (K_A , where $K_A > 0$) and the factor by which nucleotide binding favours channel closure (D , where $D < 1$).

Our simultaneous binding and current measurements were well fit with a Monod-Wyman-Changeux (MWC)-type model (Figure 2D,E; *Monod et al. (1965)*) which has been previously proposed to explain K_{ATP} channel inhibition (*Enkvetachakul and Nichols, 2003; Craig et al., 2008; Vedovato et al., 2015*). In our MWC-type model, each ligand binding event (K_A) is independent and each bound ligand favours the closed state by the same factor (D). Simultaneous measurement of binding (fluorescence) and gating (current) allowed us to obtain well constrained fits to our model. To obtain free parameter (L , K_A , D) estimates and verify that each parameter was well and uniquely determined, we employed a Bayesian Markov chain Monte Carlo (MCMC) method previously employed by Hines et al. (*Hines et al., 2014*). Using this approach, we constructed posterior probability distributions for the free parameters of our MWC-type model (Figure 2F, Table 3). Based on these distributions, we estimated $K_A = 2.1 \times 10^4 \text{ M}^{-1}$ ($K_D = 47.9 \mu\text{M}$), $L = 0.09$ ($P_{open} = 0.08$), and $D = 0.04$. The very low D value indicates that nucleotide binding was tightly coupled to channel closure; i.e. nucleotides have a very strong preference for the closed state of the channel. The low value for D also explains why the channels were nearly completely inhibited at TNP-ATP concentrations at which not all the binding sites were occupied, as well as the degree to which channel inhibition is complete at saturating concentrations of TNP-ATP. Our estimate of L was quite low and broadly distributed. We repeated our fits with L fixed to a value consistent with previous single channel measurements (0.8, $P_{open} = 0.45$, *John et al. (1998); Enkvetachakul et al. (2000); Ribale et al. (2006)*). This had only a very small effect on our estimates of D and K_A (Figure 2—Figure supplement 1). The broad distribution of L in our fit may represent current rundown which

occurs during our patch-clamp recordings and is expected to affect the open-closed equilibrium. Cross-correlation plots (in parameter space) of the values derived from our fits produced well bounded ellipsoids, indicating that our parameters were uniquely determined (Figure 2—Figure supplement 1A).

In addition to the full MWC-type model we considered alternate models (Figure 2—Figure supplement 2). These included a model in which only the first binding event influences the open-closed equilibrium of the channel (single-binding model; Figure 2—Figure supplement 2B, Table 3), and an MWC-style model with an additional parameter C to allow for direct negative cooperativity between binding sites (negative cooperativity model; Figure 2—Figure supplement 2C, Table 3). The single-binding model yielded very similar parameter estimates to our full MWC-type model (Figure 2—Figure supplement 2D, Table 3). This is a consequence of D being so low that even in the MWC-type model most channels are closed when only a single nucleotide is bound. The cooperative model improved our fits, but not enough to justify the inclusion of an additional free parameter (see Discussion).

Kir6.2-C166S affects the ability of bound nucleotides to close K_{ATP}. To provide a rigorous test as to whether our experimental system was capable of separating nucleotide binding from subsequent channel gating, we introduced a mutation (Kir6.2-C166S) which increases P_{open} of K_{ATP} and decreases sensitivity of the channel to inhibition by nucleotides (*Trapp et al., 1998*). C166 is located near the bundle-crossing gate of Kir6.2 (Figure 3A). Other mutations at this site cause neonatal diabetes (*Flanagan et al., 2006*; *Gloyn et al., 2006*).

In unroofed membranes, Kir6.2*,C166S-GFP + SUR1 bound TNP-ATP with an EC_{50} very similar to that of Kir6.2*-GFP + SUR1 (Figure 3B, 32.0 μM and 25.6 μM, respectively), which suggests only a small change in nucleotide affinity. This is an unexpected finding, as one might expect that an increase in P_{open} would allosterically cause a decrease in the apparent affinity for inhibitory nucleotide binding. To resolve this conflict, we again turned to PCF (Figure 3C,D). Rundown was much slower for Kir6.2*,C166S-GFP + SUR1, which

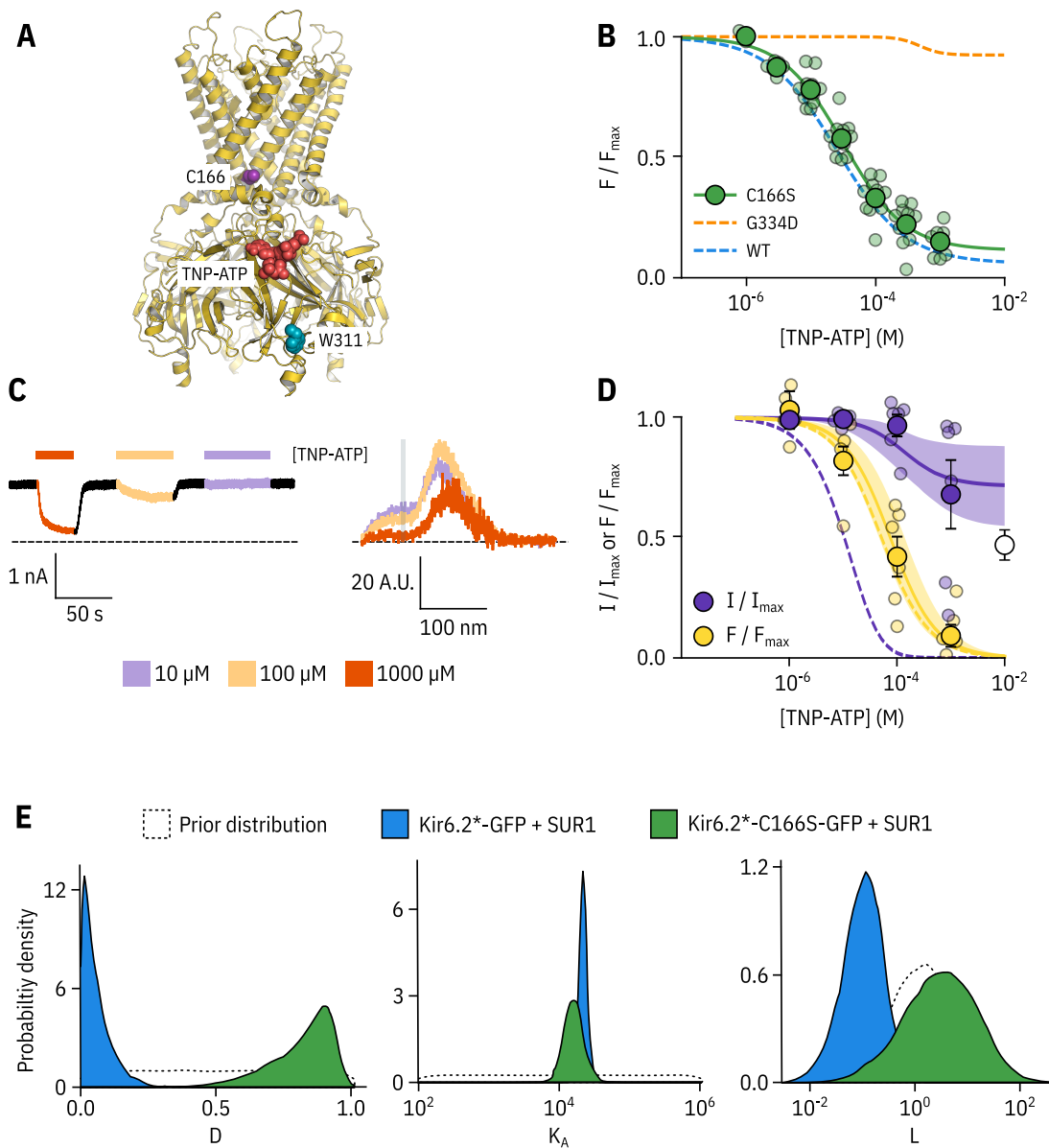


Figure 3. Kir6.2-C166S disrupts current inhibition, not nucleotide binding.

Figure 3. Kir6.2-C166S disrupts current inhibition, not nucleotide binding. **A.** Cartoon (from PDB accession #6BAA) showing the location of Kir6.2-C166 (purple) relative to the inhibitory nucleotide binding site (TNP-ATP from PDB accession #5XW6 shown in red). W311 is shown as blue spheres. **B.** Concentration dependence of TNP-ATP binding to unroofed membrane fragments expressing Kir6.2*,C166S-GFP + SUR1 shown in green, expressed as quenching of ANAP fluorescence. The Hill fits shown previously for Kir6.2*-GFP + SUR1 and Kir6.2*,G334D-GFP + SUR1 are shown in blue and orange dashed curves, respectively. Kir6.2*,C166S-GFP + SUR1: $EC_{50} = 32.0 \mu\text{M}$, $h = 0.92$, $E_{max} = 0.96$, $n = 12$. **C.** Representative current and fluorescence traces recorded simultaneously from an excised patch expressing Kir6.2*,C166S-GFP + SUR1. Exposure to different concentrations of TNP-ATP are shown by colour. **D.** Concentration-response ($n = 6$) for TNP-ATP inhibition of Kir6.2*,C166S-GFP + SUR1 currents (I/I_{max}) and for quenching of ANAP fluorescence (F/F_{max}). Data were fit with the MWC-type model. Solid curves represent the median fits and shaded areas indicate the 95% quantile intervals. Dashed curves represent the previous median fits of the MWC-type model to the Kir6.2*-GFP + SUR1 data from Figure 2D. Parameter estimates are reported in Table 3. The open data point represents current inhibition by 10 mM ATP and was not included in the model fitting. **E.** Posterior probability distributions for the full MWC-type model fit to Kir6.2*,C166S-GFP + SUR1 or Kir6.2*-GFP + SUR1 (data from Figure 2F) overlaid on the prior probability distribution.

Figure 3 – figure supplement 1. Fixing the L parameter does not affect the other two parameters.

Figure 3 – figure supplement 2. An MWC-type model predicts a nucleotide insensitive plateau of current for Kir6.2-C166S.

may reflect the increased P_{open} of this construct. Measuring current inhibition in combination with nucleotide binding confirmed that whereas the apparent nucleotide affinity was unchanged by the C166S mutation, current inhibition occurred at much higher concentrations compared to binding (Figure 3D). How can we explain this paradox? Fits of the data with our MWC-type model (Figure 3D,E) suggest that, in addition to the expected effect on L , the C166S mutation profoundly affects the ability of bound ligand to stabilise the closed state of the channel (D) without affecting K_A (Figure 3E, Table 3). We propose that, in addition to increasing the P_{open} of the channel, C166 is also important in the transition pathway from the inhibitory nucleotide binding site on Kir6.2 to the channel gate.

Our MWC-type model predicts a nucleotide-insensitive current plateau at high concentrations, with the height of the plateau at saturating nucleotide concentrations given by $\frac{L \cdot D^4}{1+L \cdot D^4}$. For example, when $L \cdot D^4 = 0.05$ we see a current plateau of just under 5%, and as $L \cdot D^4$ increases so does the plateau (Figure 3-Figure supplement 2C,D). We were unable to test inhibition of Kir6.2*,C166S-GFP + SUR1 by TNP-ATP concentrations of over 1 mM as our stocks of TNP-ATP are prepared from triethylammonium salts, and triethylamine concentrations of over 1 mM are sufficient to inhibit K_{ATP} and influence our results (Figure 3-Figure supplement 2A,B). However, we see only partial inhibition of Kir6.2*,C166S-GFP + SUR1 by 10 mM ATP which supports the existence of a plateau. This observation has been previously reported for mutations at Kir6.2-C166 in some constructs (Trapp et al., 1998; Ribalet et al., 2006) but not others (Enkvetchakul et al., 2001).

Exploring the effect of SUR1 on nucleotide inhibition of K_{ATP} . SUR1 plays a complex role in the regulation of Kir6.2. It increases the P_{open} of the channel and allows for the activation of the channel by Mg-nucleotides (Nichols et al., 1996; Tucker et al., 1997; Babenko and Bryan, 2003; Chan et al., 2003; Fang et al., 2006). However, it also increases the sensitivity of Kir6.2 to nucleotide inhibition (Babenko and Bryan, 2003; Chan et al., 2003; Fang et al., 2006). To understand the effect of SUR1 on nucleotide inhibition of K_{ATP} , we expressed Kir6.2*-GFP in the absence of SUR1 in unroofed membranes and measured TNP-ATP binding (Figure 4-Figure supplement 1A). We found only a small in-

crease (approximately 1.5-fold) in apparent EC_{50} compared to the same construct in the presence of SUR1 (37.6 μ M and 25.6 μ M respectively). Unfortunately, we were unable to achieve high enough expression of Kir6.2*-GFP alone to carry out PCF experiments in the absence of SUR1. However, we were able to measure currents from unlabelled Kir6.2-GFP alone (Figure 4-Figure supplement 1B). As expected Kir6.2-GFP alone was much less sensitive to inhibition by TNP-ATP than Kir6.2-GFP + SUR1.

As Kir6.2*-GFP expression in the absence of SUR1 was not sufficient for PCF recordings, we took a mutational approach to better understand the role of SUR1 in inhibitory nucleotide binding. SUR1-K205 is located in the L0 linker of SUR1, which connects the first set of transmembrane domains (TMD0) to the ABC core structure (Figure 1A, Figure 4A; *Martin et al. (2017); Puljung (2018)*). This loop is adjacent to the inhibitory nucleotide-binding site on Kir6.2 and the interface between neighbouring Kir6.2 subunits. Mutations at SUR1-K205 were previously shown to reduce sensitivity of K_{ATP} to nucleotide-dependent inhibition (*Pratt et al., 2012; Ding et al., 2019*), and a recent cryo-EM structure suggests that SUR1-K205 may directly coordinate the phosphates of ATP bound to Kir6.2 (*Ding et al., 2019*). Other mutations in L0 are associated with neonatal diabetes (*Ashcroft et al., 2017*) and PHHI (*Snider et al., 2013*).

We introduced a charge neutralization (alanine, K205A) and a charge reversal (glutamate, K205E) mutation at this position and measured simultaneous nucleotide binding and current inhibition with PCF (Figure 4B,C,D). The binding and inhibition curves for TNP-ATP almost perfectly overlaid for the SUR1-K205A mutant (Figure 4C). The same was also true for SUR1-K205E (Figure 4D). Data were fit with the MWC-type model as before. Mutating K205 to an alanine or a glutamate resulted in an apparent decrease in nucleotide binding affinity (Figure 4C,D,E). This was reflected by a decrease in the estimated K_A for TNP-ATP, which correlated with the degree of conservation of the mutation, i.e. we observed a larger effect for the charge reversal compared to the charge neutralization mutation (Figure 4E). However, in addition to direct effects of K205 on nucleotide binding, we also observed a shift in D for both mutations (Figure 4E). This suggests a dual role for

285 SUR1 in K_{ATP} inhibition, both in contributing to nucleotide binding and in stabilizing the
286 nucleotide-bound closed state.

Discussion

288 We have developed a novel approach that allows for site-specific measurement of nu-
289 cleotide binding to K_{ATP} and concomitant measurements of channel current. Perform-
290 ing these measurements simultaneously allowed us to examine nucleotide regulation of
291 K_{ATP} function in great detail. We used a Bayesian approach to fit models to our combined
292 fluorescence/current data sets to extract meaningful functional parameters with a min-
293 imum of prior assumptions. Such insights would not be possible from experiments in
294 which macroscopic currents or binding were measured in isolation.

295 PCF has been used successfully by other labs to simultaneously measure ligand bind-
296 ing and gating in HCN channels (*Biskup et al., 2007; Kusch et al., 2010; Wu et al., 2011*).
297 These groups measured fluorescence from a cyclic nucleotide analogue that increased its
298 quantum yield when bound, minimizing background fluorescence from unbound ligand.
299 Additional background subtraction could be performed by imaging the patches using
300 confocal microscopy such that a region corresponding to the patch membrane could be
301 computationally selected, thus omitting background fluorescence from the surrounding
302 solution (*Biskup et al., 2007; Kusch et al., 2010*). In our PCF experiments, we used a FRET-
303 based approach to measure ligand binding. We acquired fluorescence emission spectra,
304 such that donor fluorescence could be separated from acceptor fluorescence by wave-
305 length. This allowed us to directly assess binding from the quenching of donor fluores-
306 cence, which was specific to K_{ATP}. FRET also provided the spatial sensitivity necessary to
307 discriminate between nucleotide binding directly to Kir6.2 and to the nucleotide-binding
308 sites of SUR1. We assume that any TNP-ATP bound non-specifically to our membranes
309 would be too far from Kir6.2 to cause appreciable FRET. This assumption was confirmed
310 by the lack of FRET between TNP-ATP and a Kir6.2*-GFP mutant (G334D), in which nu-
311 cleotide binding was severely disrupted (Figure 1H).

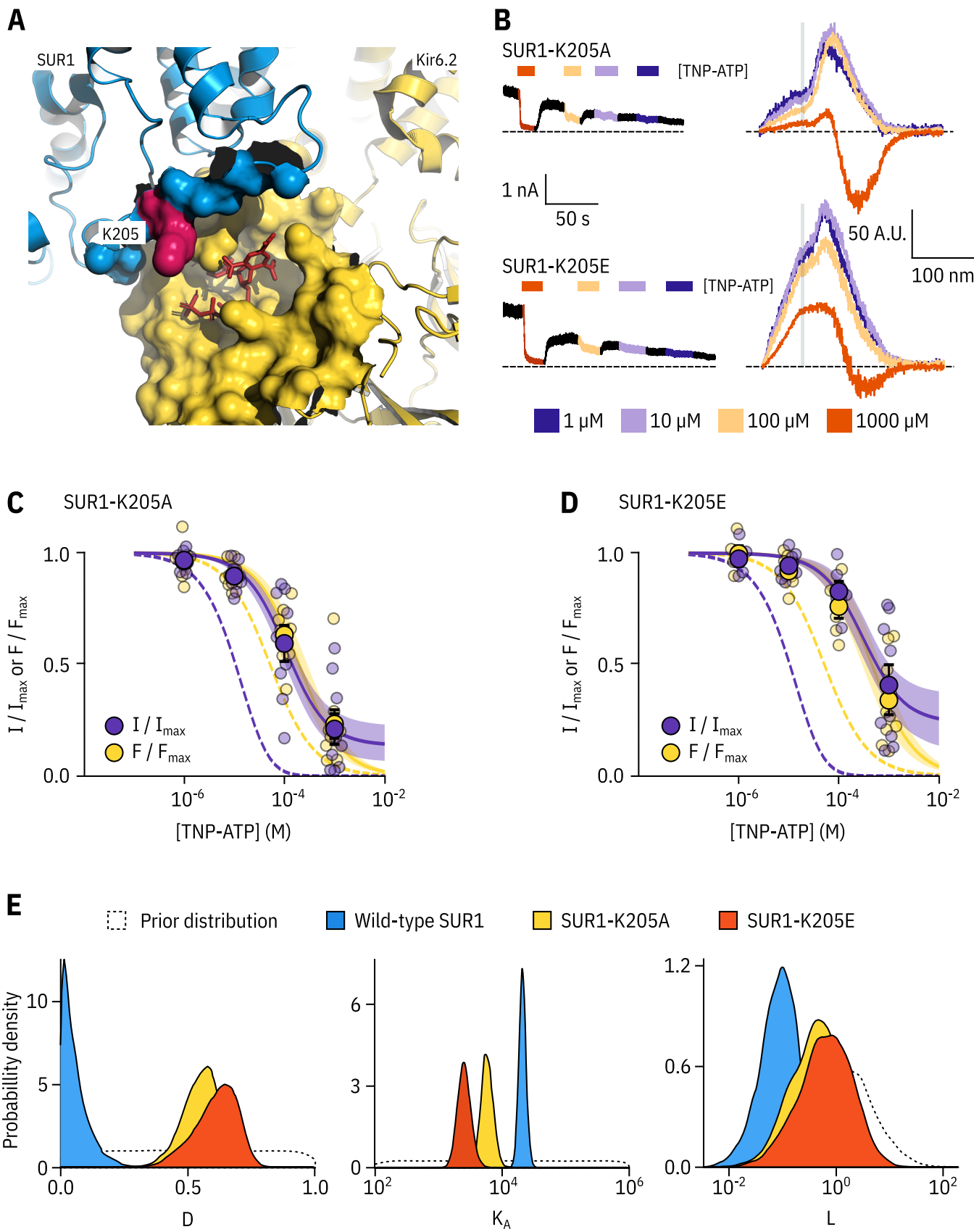


Figure 4. SUR1-K205 modulates both nucleotide affinity and inhibition of Kir6.2.

Figure 4. SUR1-K205 modulates both nucleotide affinity and inhibition of Kir6.2. **A.** Hydrophobic surface representation of Kir6.2 (yellow, PDB accession #6BAA) and SUR1 (blue, PDB accession #6PZI). Residue K205 on SUR1 is highlighted in pink. As this residue was built as an alanine in the structure, we used the mutagenesis tool in PyMol to insert the native lysine residue. A docked TNP-ATP molecule is shown in red. **B.** Representative current and fluorescence traces acquired simultaneously from excised patches expressing Kir6.2*-GFP with SUR1-K205A or SUR1-K205E. **C,D.** Concentration-response for TNP-ATP inhibition of currents (I/I_{max}) and for quenching of ANAP fluorescence (F/F_{max}) in excised inside-out membrane patches expressing Kir6.2*-GFP + SUR1-K205A (**C**, $n = 9$) or Kir6.2*-GFP + SUR1-K205E (**D**, $n = 9$). Data were fit to the MWC-type model. Solid curves represent the median fits and shaded areas indicate the 95% quantile intervals. Fits to Kir6.2*-GFP + wild-type SUR1 are shown as dashed curves. **E.** Posterior probability distributions for the full MWC-type model fit to Kir6.2*-GFP co-expressed with wild-type SUR1 (fits from Figure 2), SUR1-K205A and SUR1-K205E overlaid on the prior probability distribution.

Figure 4 – figure supplement 1. SUR1 affects the apparent affinity for nucleotide binding to Kir6.2.

Figure 4 – figure supplement 2. Fixing the L parameter does not drastically affect the fits to the SUR1-K205A or SUR1-K205E data.

Figure 4 – figure supplement 3. Comparing the ability of each model to explain the data.

Figure 4 – figure supplement 4. A neutral choice of priors allows for the best fits to the data.

312 Previous studies have suggested that K_{ATP} inhibition follows an MWC-type model (*Trapp*
 313 *et al., 1998; Enkvetachakul and Nichols, 2003; Drain et al., 2004; Craig et al., 2008; Ve-*
 314 *dovato et al., 2015*). The majority of this earlier work was performed using single-channel
 315 measurements of mutated and/or concatenated channel subunits. In this study, we con-
 316 firm these results using minimally perturbed channels with nucleotide sensitivity similar
 317 to that of wild-type K_{ATP} (Figure 1—Figure supplement 2A). By using an MCMC approach
 318 to model fitting, we can also evaluate our models to assess how well the derived param-
 319 eters were determined by the data. MCMC fits provide a basis for determining credible
 320 intervals for our parameter estimates. This allows for direct comparison of values de-
 321 rived from wild-type and different mutant constructs.

322 Although we did not explicitly include the effects of PIP_2 on K_{ATP} gating in our model
 323 formulations, we assumed that the effects of PIP_2 on P_{open} were implicitly modelled in our
 324 parameter L ; i.e. rundown due to dissociation of PIP_2 manifests as a decrease in L rather
 325 than a change in the number of channels. Although we were able to extract identifiable
 326 parameter estimates for L , D and K_A , our estimates of L for each model we considered
 327 were appreciably less well constrained than for the other parameters. We expect that
 328 this uncertainty arises from measuring a heterogeneous population of channels with
 329 regard to PIP_2 binding. Fixing L to values obtained from the literature (Figure 2—Figure
 330 supplement 1, Figure 3—Figure supplement 1, Figure 4—Figure supplement 2, Figure 4—
 331 Figure supplement 3) allowed us to extract estimates for D and K_A that were functionally
 332 identical to those derived from unconstrained fits, suggesting that the uncertainty of L
 333 does not affect our inferences for these other parameters. Although the value for L that
 334 we obtained from the literature for Kir6.2*-GFP + SUR1 (0.8) is on the extreme end of the
 335 posterior probability distribution for L from our fits, we would not expect it to change our
 336 estimates of K_A or D as these values were stable over a broad range of values of L (Figure
 337 2—Figure supplement 1) for this construct. Therefore, PCF represents a robust means to
 338 compare K_A and D between different mutated K_{ATP} constructs without worrying about
 339 the confounding effects of rundown.

340 Previous studies suggest that, whereas K_{ATP} closure occurs via a concerted mecha-
 341 nism, individual nucleotide binding events at Kir6.2 are not equivalent (*Markworth et al.*,
 342 **2000**). Earlier attempts to determine the stoichiometry of inhibitory nucleotide binding
 343 to Kir6.2 (i.e. how many ATPs must bind to induce channel closure) have produced mod-
 344 els ranging from those in which binding of a single nucleotide completely shuts K_{ATP} to
 345 an MWC-type model in which each binding event is independent and contributes equally
 346 to channel closure (*Trapp et al., 1998; Markworth et al., 2000; Enkvetachakul and Nichols,*
 347 *2003; Drain et al., 2004; Wang et al., 2007; Craig et al., 2008; Vedovato et al., 2015*). To
 348 resolve this controversy, we fit our data with both single-binding and MWC-type models.
 349 At very low values for D , such as we derived from our experiments, the predictions of
 350 both models are functionally very similar. Even in our MWC-type model, we expect most
 351 K_{ATP} channels to be closed when just one molecule of nucleotide is bound.

352 It has been proposed that there is direct negative cooperativity between binding events
 353 at different subunits on Kir6.2 (*Wang et al., 2007*). We fit our data to an extended MWC-
 354 type model including an additional free parameter (C), representing negative binding
 355 cooperativity between subunits (Figure 2—Figure supplement 2). Not surprisingly this
 356 model improved the fit to our data as assessed by the Bayes factor, which represents the
 357 marginal likelihood of one model over another to explain our observations (*Wagenmak-*
 358 *ers, 2007; Gronau et al., 2017*). We also tested the cooperative model using approximate
 359 leave-one-out cross validation, which assesses the ability of a model to predict new or
 360 out-of-sample data using in-sample fits (*Vehrtari et al., 2017*). Although in this work, we
 361 are primarily concerned with the inferences made from our fits, the ability of a model to
 362 make predictions is a good measure of its usefulness. Based on this criterion, the coop-
 363 erative model has no more predictive accuracy than either the MWC-type model or the
 364 single-binding model. Therefore, the inclusion of an additional free parameter is not jus-
 365 tified. Furthermore, whereas the cooperative model yielded good fits with identifiable
 366 parameters for Kir6.2*-GFP + SUR1 channels, it failed to yield identifiable parameters
 367 for all the mutants considered. Thus, this model did not allow for direct comparison be-

³⁶⁸ tween constructs. However, it remains a possibility that these mutations function in part
³⁶⁹ by abolishing binding cooperativity between subunits.

³⁷⁰ We performed all our experiments on mutated, tagged channels using a fluorescent
³⁷¹ derivative of ATP. This allowed us to fit mechanistic models and readily compare between
³⁷² mutated constructs that affect nucleotide inhibition of K_{ATP}. This raises an obvious ques-
³⁷³ tion: how relevant are our findings to inhibition of wild-type K_{ATP} by ATP? In a previous
³⁷⁴ paper, we estimated *D* and *K_A* from an MWC-type model based on fits to published data
³⁷⁵ for ATP inhibition of wild-type Kir6.2 + SUR1 (*Proks et al., 2010; Vedovato et al., 2015*).
³⁷⁶ The value we obtained for *D* (0.03) was quite similar to that we report here from our PCF
³⁷⁷ measurements (0.04). We also obtained a similar estimate for *K_A* in our previous model
³⁷⁸ ($3.0 \times 10^4 \text{ M}^{-1}$ vs $2.1 \times 10^4 \text{ M}^{-1}$ from our PCF experiments). Despite obtaining similar pa-
³⁷⁹ rameters, past experiments in which only ionic currents were measured, did not allow us
³⁸⁰ to distinguish between competing gating models. Measuring currents and fluorescence
³⁸¹ simultaneously allowed for better model selection and aided in our ability to identify con-
³⁸² strained parameters.

³⁸³ We compared the parameters derived for inhibitory nucleotide binding to those esti-
³⁸⁴ mated for nucleotide activation of K_{ATP} based on experiments in which currents and bind-
³⁸⁵ ing were measured in separate preparations (*Puljung et al., 2019*). In those experiments,
³⁸⁶ we estimated a value for *E*, the factor by which binding of MgTNP-ADP to SUR1 stabilized
³⁸⁷ channel opening, of 2.2. Although this value was derived using a different nucleotide, it
³⁸⁸ still provides an approximate basis for comparing the coupling of nucleotide stimulation
³⁸⁹ through SUR1 to nucleotide inhibition via binding to Kir6.2. If both activation and inhibi-
³⁹⁰ tion proceed via MWC-type models, the open closed equilibrium at saturating nucleotide
³⁹¹ concentrations is given by *L* multiplied by *E*⁴ or *D*⁴, respectively. The degree of stabiliza-
³⁹² tion of the open state of K_{ATP} can be calculated as $-RT \ln E^4$ for activation. Stabilization
³⁹³ of the closed state is given by $-RT \ln D^4$. Based on our observations, saturating concen-
³⁹⁴ trations of MgTNP-ADP stabilized the open state by $-1.9 \text{ kcal mol}^{-1}$ (-7.9 kJ mol^{-1}). At
³⁹⁵ saturating concentrations, TNP-ATP stabilized the closed state of K_{ATP} by $-7.6 \text{ kcal mol}^{-1}$

(31.8 kJ mol⁻¹). Thus, assuming excitatory and inhibitory processes are independent, inhibition would be expected to dominate under conditions at which all the nucleotide binding sites are occupied. This is consistent with published measurements of wild-type K_{ATP} in the presence of Mg²⁺ (*Proks et al. (2010)*). In our previous study, we estimated K_A for MgTNP-ADP binding to the stimulatory second nucleotide binding site of SUR1 to be 5.8×10^4 M⁻¹ ($K_D = 17$ μM), higher affinity than the K_A we report here for TNP-ATP binding to the inhibitory site on Kir6.2 (2.1×10^4 M⁻¹, $K_D = 48$ μM). Higher affinity binding to the stimulatory site may explain the ability of MgADP to increase K_{ATP} currents in the presence of ATP (*Gribble et al., 1998*). This phenomenon may also explain the bell-shaped MgADP concentration-response curve for K_{ATP} , which shows an increase in current at low concentrations, followed by inhibition at higher concentrations (*Proks et al., 2010; Vedovato et al., 2015*). Future experiments in which activation and inhibition are measured by PCF for the same ligand will allow us to model the complex response of K_{ATP} under conditions where all three nucleotide binding sites simultaneously affect channel gating (i.e. in the presence of Mg²⁺).

Mutations that cause neonatal diabetes reduce the sensitivity of K_{ATP} to nucleotide inhibition, and reduction in nucleotide sensitivity is broadly correlated with disease severity (*McTaggart et al., 2010*). We studied two residues on Kir6.2 that have been implicated in diabetes and have been proposed to affect nucleotide sensitivity via different mechanisms. We find that G334D drastically reduced the apparent affinity for nucleotide binding to K_{ATP} in unroofed membranes. In our MWC-type models, this could only be explained by a dramatic decrease in K_A . This corroborates earlier hypotheses that mutating G334 directly disrupts inhibitory nucleotide binding to Kir6.2 (*Drain et al., 1998*). Due to poor expression, we were unable to test this construct using PCF. Therefore, we could not obtain accurate estimates of K_A and D .

In contrast to G334D, the C166S mutation does not directly affect nucleotide binding to Kir6.2, but rather disrupts the ability of bound nucleotide to close the channel. This contributes to the decreased nucleotide sensitivity which was previously attributed solely

424 to an increased P_{open} . In the future, we hope to use this rigorous approach to assess a
425 whole panel of neonatal diabetes mutations in Kir6.2 to better understand the mecha-
426 nism by which they cause disease.

427 Using PCF allowed us to probe more deeply into the role of SUR1 in regulating nu-
428 cleotide inhibition of K_{ATP} . The cytoplasmic L0 loop of SUR1 was previously implicated
429 in modulation of P_{open} and nucleotide sensitivity of Kir6.2 (**Babenko and Bryan, 2003;**
430 **Chan et al., 2003; Pratt et al., 2012**). We find that, in addition to directly contributing
431 to tighter nucleotide binding at Kir6.2, SUR1 plays a critical role in preferentially stabil-
432 ising the closed state of the channel when nucleotides are bound. Whereas a single
433 nucleotide-binding event is sufficient for channel closure when Kir6.2 is associated with
434 wild-type SUR1, mutating residue K205 reduced the ability of a single nucleotide to close
435 the channel. This difference manifests in both our MWC-type and single-binding models.

436 In addition to providing mechanistic insights into disease-associated mutations in
437 Kir6.2, our PCF-based approach allows us to probe the interactions between Kir6.2 and
438 SUR1 on two different levels. As we show here, we can use this method to examine the
439 effects of SUR1 on inhibitory nucleotide binding to Kir6.2. We can also adapt this method
440 to study activation of Kir6.2 by nucleotides bound to the stimulatory sites on SUR1. Mu-
441 tations in SUR1 that cause neonatal diabetes may do so by disrupting inhibitory bind-
442 ing/gating or enhancing the stimulatory effects of nucleotides. The formalism developed
443 in this study provides a rigorous way to mechanistically assess the effects of these muta-
444 tions. Our approach should be readily adaptable to the study of other nucleotide-gated
445 channels including the cystic fibrosis transmembrane conductance regulator (CFTR, also
446 an ABC-family protein) and purinergic P2X receptors.

Materials and Methods

448 Key resources table.

Reagent type(species) or resource	Designation	Source or reference	Identifiers	Additional information
Cell line	HEK-293T (H. sapiens) pANAP	LGC Standards (ATCC CRL-3216) Addgene		
Transfected construct (<i>Escherichia. coli</i>)	pcDNA4/TO	Addgene		
Transfected construct	pCGFP_EU	Gouaux Laboratory (Vollum Institute, Portland OR USA)		
Transfected construct (<i>Aequorea victoria</i>)				
Transfected construct (<i>Homo sapiens</i>)	peRF1-E55D	Chin Laboratory (MRC Laboratory of Molecular Biology, Cambridge UK)		
Antibody	Anti-HA High Affinity; Rat monoclonal antibody (clone 3F10)	Roche	(Roche Cat# 11867423001, RRID:AB_10094468)	(1:1000)
Antibody	Peroxidase-AffiniPure Goat Anti-Rat IgG (H + L) antibody	Jackson ImmunoResearch Labs	(Jackson ImmunoResearch Labs Cat# 112-035-003, RRID:AB_2338128)	Western blots: (1:20,000) Surface expression: (1:2000)
Chemical drug	trinitrophenyl-ATP (TNP-ATP)	Jena Bioscience (Jena, Germany)		
Chemical drug	L-3-(6-acetyl naphthalen-2-ylamino)-2-aminopropionic acid	Asis Chemicals (Waltham, MA)		

450 Molecular biology.

451 Human Kir6.2 and SUR1 were subcloned into pcDNA4/TO and pCGFP_EU vectors for ex-
 452 pression of wild-type and GFP-tagged constructs, respectively. pcDNA4/TO and pANAP
 453 were obtained from Addgene. peRF1-E55D and pCGFP_EU were kind gifts from the Chin
 454 Laboratory (MRC Laboratory of Molecular Biology, Cambridge, UK) and the Gouaux Lab-
 455 oratory (Vollum Institute, Oregon, USA) respectively. Amber stop codons and point mu-
 456 tations were introduced using the QuikChange XL system (Stratagene; San Diego, CA). All
 457 constructs were confirmed by DNA sequencing (DNA Sequencing and Services, University
 458 of Dundee, Scotland).

459 Cell culture and channel expression.

460 HEK-293T cells were obtained from and verified/tested for mycoplasma by LGC standards
 461 (ATTC CRL-3216, Middlesex, UK). Our working stock tested negative for mycoplasma con-
 462 tamination using the MycoAlert Mycoplasma Detection Kit (Lonza Bioscience; Burton on
 463 Trent, UK). Cells were plated onto either poly-L-lysine coated borosilicate glass coverslips
 464 (VWR International; Radnor, PA) or poly-D-lysine coated glass-bottomed FluoroDishes
 465 (FD35-PDL-100, World Precision Instruments). ANAP-tagged Kir6.2 constructs were la-
 466 belled using amber stop codon suppression as described by Chatterjee et al (*Chatterjee*
 467 *et al., 2013*). Transfections were carried out 24 hours after plating using TransIT-LT1
 468 (Mirus Bio LLC; Madison, WI) at a ratio of 3 μ l per μ g of DNA. Unless specified otherwise,
 469 all transfections included a Kir6.2 construct with an amber stop codon (TAG) at position
 470 311 (Kir6.2-W311^{TAG}), SUR1, pANAP and eRF1-E55D in the ratio 0.5:1.5:1:1. Transfected
 471 cells cultured in Dulbecco's Modified Eagle Medium (Sigma; St. Louis, MO) + 10% foetal
 472 bovine serum, 100 U ml⁻¹ penicillin and 100 μ g ml⁻¹ streptomycin (Thermo Fisher Scien-
 473 tific; Waltham, MA) supplemented with 20 mM ANAP (free acid, AsisChem; Waltham, MA).
 474 Cells were incubated at 33 °C and in the presence of 300 μ M tolbutamide to enhance
 475 protein expression and channel trafficking to the plasma membrane (*Yan et al., 2007*;
 476 *Lin et al., 2015*). eRF1-E55D was included to increase efficiency of ANAP incorporation
 477 (*Schmied et al., 2014*). Experiments were carried out 2-4 days after transfection. We also
 478 expressed constructs labelled with ANAP at positions I182, F183, F198, and I210. Kir6.2-
 479 F183*, Kir6.2-F198*, and Kir6.2-I210* co-expressed with SUR1 did not produce sufficient
 480 currents for subsequent experimentation. Mutations at I182 are known to produce pro-
 481 found effects on nucleotide inhibition of K_{ATP} (*Li et al., 2000*). Thus, we did not consider
 482 this site for further experimentation.

483 Western blots.

484 Transfected HEK-293T cells grown in 6-well plates were harvested in cold PBS (Life Tech-
 485 nologies Limited; Paisley, UK), pelleted at 0.2 x g for 2.5 minutes and resuspended in lysis

486 buffer containing 0.5% Triton X-100, 100 mM potassium acetate, and a cOmplete pro-
487 tease inhibitor tablet (1 tablet/50 ml, Roche; Basel, Switzerland), buffered to pH 7.4. Af-
488 ter a 30-minute benzonase (Sigma) treatment at room temperature, samples were mixed
489 with a DTT containing reducing agent and loading buffer (NuPAGE, Invitrogen; Carlsbad,
490 CA) and run on a precast Bis-Tris 4-12% poly-acrylamide gel at 200 V for 40 minutes. Pro-
491 teins were wet transferred overnight onto polyvinylidene difluoride (PVDF) membranes
492 (Immobilon P, Merck Millipore; Burlington, VT) in 25 mM Tris, 192 mM glycine, 20% methanol,
493 and 0.1% SDS at 10 V on ice. Membranes were blocked with 5% milk in TBS-Tw (150 mM
494 NaCl, 0.05% Tween 20, 25 mM Tris, pH 7.2) before staining for 30 minutes with a 1:1000
495 dilution of rat anti-HA monoclonal antibody in TBS-Tw (clone 3F10, Roche). After washing
496 with TBS-Tw, membranes were incubated for 30 minutes with a 1:20,000 dilution of HRP-
497 conjugated goat anti-rat polyclonal antibodies in TBS-Tw (Jackson ImmunoResearch; Ely,
498 UK). Detection was performed using the SuperSignal West Pico Chemiluminescent Sub-
499 strate (Thermo Fisher) and a C-DiGit Blot Scanner (Licor Biosciences; Lincoln, NE). Analysis
500 was performed using custom code written in Python.

501 To confirm our ability to express full-length Kir6.2*-GFP, we performed western blots
502 for HA-tagged Kir6.2 constructs in detergent-solubilized HEK-293T cells (Figure 1—Figure
503 supplement 1C). The HA tag plus a short linker (YAYMEKGITDLAYPYDVPDY) was inserted
504 in the extracellular region following helix M1 of Kir6.2 between L100 and A101. Transfec-
505 tion of wild-type Kir6.2-HA or Kir6.2-HA-GFP resulted in two bands on the western blots.
506 The upper bands were close to the expected sizes for full-length Kir6.2-HA and Kir6.2-HA-
507 GFP (46 kDa and 77 kDa, respectively).

508 We consistently observed a lower molecular weight band as well. This band must cor-
509 respond to an N-terminally truncated Kir6.2 product, as the apparent molecular weight
510 shifted with addition of the C-terminal GFP tag. Based on the molecular weight, we pre-
511 dict that the truncated protein product initiated from a start codon in the first transmem-
512 brane domain. Therefore, we believe it is unlikely that this protein would form func-
513 tional channels or traffic to the plasma membrane. When Kir6.2-W311^{TAG}-HA or Kir6.2-

514 W311^{TAG}-HA-GFP were co-transfected with SUR1, pANAP, and eRF1-E55D, and cells were
 515 cultured in the presence of ANAP, the western blots were similar to wild-type Kir6.2-HA
 516 or Kir6.2-HA-GFP. Over 90% full-length Kir6.2*-HA-GFP was produced under these condi-
 517 tions (Figure 1—Figure supplement 1D). We were unable to quantify the percentage of
 518 full-length Kir6.2*-HA produced as the C-terminally truncated band resulting from termi-
 519 nation at the TAG codon was very similar in size to the N-terminally truncated band. Co-
 520 expression with SUR1 increased the percentage of full-length Kir6.2*-HA-GFP produced
 521 (Figure 1—Figure supplement 1D). In the absence of ANAP, we did not observe any full-
 522 length Kir6.2, indicating that there was no read-through of the amber (TAG) stop codon
 523 (Figure 1—Figure supplement 1D).

524 **Confocal microscopy.**

525 Confocal imaging was performed using a spinning-disk system (Ultra-VIEW VoX, PerkinElmer;
 526 Waltham, MA) mounted on an IX81 microscope (Olympus; Southend-on-Sea, UK) with
 527 a Plan Apo 60x oil immersion objective (NA = 1.4), provided by the Micron Advanced
 528 Bioimaging Unit, Oxford. Transfected HEK-293T cells were incubated for 15 minutes with
 529 1 nM CellMask Deep Red (Thermo Fisher) to stain plasma membranes before washing
 530 with PBS and imaging. ANAP was excited with a solid-state laser at 405 nM. GFP and Cell-
 531 Mask were excited with an argon laser at 488 nM and 633 nM respectively. Images were
 532 captured on an EMCCD camera (ImagEM; Hamamatsu Photonics; Welwyn Garden City,
 533 UK) binned at 2 x 2 pixels and analysed using Python. A median filter with a box size of
 534 32 x 32 pixels was applied to improve the signal-to-noise ratio by reducing background
 535 fluorescence.

536 We examined the surface expression of our ANAP-labelled constructs using confo-
 537 cal microscopy (Figure 1—Figure supplement 1A,B). When Kir6.2-W311^{TAG}-GFP was co-
 538 transfected with SUR1 along with pANAP and eRF1-E55D in the presence of ANAP, the
 539 ANAP and GFP fluorescence were co-localized at the plasma membrane. When wild-type
 540 Kir6.2-GFP was transfected under the same conditions, only GFP fluorescence was ob-

541 served at the plasma membrane. ANAP fluorescence was diffuse and confined to the
 542 cytoplasm or intracellular structures. Thus, the plasma-membrane ANAP signal was spe-
 543 cific for Kir6.2*-GFP.

544 **Surface expression assays.**

545 We measured surface expression of HA-tagged Kir6.2 subunits using an approach out-
 546 lined by Zerangue et al. (*Zerangue et al., 1999; Puljung et al., 2019*). Cells were plated
 547 on 19 mm coverslips coated with poly-L-lysine and transfected as described above. Fol-
 548 lowing incubation, cells were rinsed with PBS before fixation with 10% formalin for 30
 549 minutes at room temperature. After washing again, cells were blocked with 1% BSA in
 550 PBS for 30 minutes at 4 °C before a 1-hour incubation at 4 °C with a 1:1000 dilution (in
 551 PBS) of rat anti-HA monoclonal antibodies. Cells were then washed 5 times on ice with
 552 1% BSA in PBS followed by a 30-minute incubation at 4 °C with a 1:2000 dilution of HRP-
 553 conjugated goat anti-rat polyclonal antibodies. Cells were washed 5 times in PBS + 1%
 554 BSA and 4 times in PBS. Coverslips were removed from the culture dishes and placed in
 555 clean, untreated dishes for measurement. 300 µl of SuperSignal ELISA Femto Maximum
 556 Sensitivity Substrate (Thermo Fisher) was added to each sample and the luminescence
 557 was measured using a Glomax 20/20 Luminometer (Promega; Madison, WI) after a 10
 558 second incubation.

559 HEK-293T cells were transfected with Kir6.2 constructs with or without a TAG stop
 560 codon corresponding to position 311. Cells were co-transfected with pANAP and eRF1-
 561 E55D in the presence or absence of SUR1 and cultured with or without ANAP. Wild-type
 562 Kir6.2-HA and Kir6.2-HA-GFP in the presence of SUR1 were included as positive controls.
 563 Kir6.2 constructs with no HA tag served as negative controls. In the presence of ANAP,
 564 we observed strong trafficking of Kir6.2*-HA-GFP to the plasma membrane, but much
 565 less trafficking of Kir6.2*-HA (Figure 1—Figure supplement 1E). When cells were cultured
 566 in the absence of ANAP, we observed little to no Kir6.2 surface expression from cells that
 567 were transfected with Kir6.2-W311^{TAG}-HA or Kir6.2-W311^{TAG}-HA-GFP, suggesting that pre-

568 maturely truncated constructs did not traffic to the plasma membrane. In the absence
569 of SUR1, surface expression was weak for both wild-type and tagged constructs, despite
570 the reported ability of Kir6.2-GFP to traffic to the plasma membrane in the absence of
571 SUR1 (*John et al., 1998; Makhina and Nichols, 1998*).

572 **Epifluorescence imaging and spectroscopy.**

573 Epifluorescence imaging and spectroscopy were performed using a Nikon Eclipse TE2000-
574 U microscope with a 60x water immersion objective (Plan Apo VC, NA = 1.2, Nikon; Kingston
575 upon Thames, UK) or a 100x oil immersion objective (Nikon, Apo TIRF, NA = 1.49). Imag-
576 ing of ANAP was performed using a 385 nm LED source (ThorLabs; Newton, NJ) with a
577 390/18 nm band-pass excitation filter, an MD416 dichroic and a 479/40 nm band-pass
578 emission filter (all from ThorLabs). GFP was imaged using a 490 nm LED source (Thor-
579 Labs) with a 480/40 nm band-pass excitation filter, a DM505 dichroic, and a 510 nm long-
580 pass emission filter (all from Chroma; Bellows Falls, VT). Fluorescence spectra were col-
581 lected by exciting ANAP as above but using a 400 nm long-pass emission filter (Thor-
582 Labs), then passing emitted light through an IsoPlane 160 Spectrometer (Princeton Instru-
583 ments; Trenton, NJ) with a 300 g mm^{-1} grating. Images were collected with 1 s exposures
584 on a Pixis 400BR_eXcelon CCD (Princeton Instruments).

585 **Electrophysiology.**

586 Patch pipettes were pulled from thick-walled borosilicate glass capillaries (GC150F-15,
587 Harvard Apparatus; Holliston, MA) to a resistance of $1.5\text{ M}\Omega$ to $2.5\text{ M}\Omega$ when filled with
588 pipette solution. Currents were recorded at -60 mV from excised inside-out patches
589 using an Axopatch 200B amplifier equipped with a Digidata 1322A digitizer and using
590 pClamp 10 software (Molecular Devices; San Jose, CA). Currents were low-pass filtered
591 at 5 kHz and digitized at 20 kHz. The bath solution (intracellular) contained 140 mM KCl,
592 10 mM HEPES, 1 mM EDTA and 1 mM EGTA (pH 7.3 with KOH). The pipette solution (extra-
593 cellular) contained 140 mM KCl, 10 mM HEPES and 1 mM EDTA (pH 7.4 with KOH). All ex-
594 periments were carried out in Mg^{2+} -free conditions. Currents were leak corrected using

595 the current remaining in bath solution containing 5 mM barium acetate at 60 mV, assum-
 596 ing a linear leak with a reversal potential of 0 mV. Inhibition was calculated and corrected
 597 for rundown by alternating test concentrations of nucleotide solution with nucleotide-
 598 free solution, then expressing the test currents as a fraction of the average of the control
 599 currents before and after the test solution as described previously (*Proks et al., 2010*).

600 FRET calculations

601 We calculated the expected FRET efficiency between ANAP incorporated at amino acid po-
 602 sition 311 and a docked TNP-ATP molecule as described previously (*Puljung et al., 2019*).
 603 The equivalency between FRET efficiency (measured as ANAP quenching) and nucleotide
 604 binding is based on two main assumptions. Firstly, we assume that the observed quen-
 605 ching from a bound nucleotide does not differ dramatically between open and closed states
 606 of the channel. As there is no open-state structure of K_{ATP}, we do not know exactly how
 607 much relative movement would occur between a bound TNP-ATP and Kir6.2-W311. How-
 608 ever, based on cryo-EM structures of apo and nucleotide-bound Kir6.2 we do not expect
 609 to see a change in the distance between these two positions (*Martin et al., 2019*).

610 Secondly, we assume that the ANAP and TNP-ATP molecules on each subunit do not
 611 undergo energy transfer with those on other subunits to an extent which would dramati-
 612 cally change the observed quenching. At saturating TNP-ATP concentrations, where each
 613 ANAP-labelled site on Kir6.2 is occupied, FRET between ANAP and the closest acceptor
 614 will be kinetically favoured and the overall FRET efficiency will not be affected by cross-
 615 talk between neighbouring sites (*Corry et al., 2005*). In the limiting case, at low TNP-ATP
 616 concentrations, one would expect a large proportion of Kir6.2 tetramers (with four ANAP-
 617 labelled binding sites) bound to only a single TNP-ATP molecule. In this case, we expect
 618 a 4% overestimation of nucleotide binding as calculated using a numerical method to
 619 simulate a single TNP-ATP acceptor with multiple ANAP donors based on the distances
 620 calculated from our docking (Figure 1C, *Deplazes et al. (2012)*). This may have resulted
 621 in our binding curves becoming artificially shallow at low concentrations. However, this

622 difference is not significant in the context of our measurements as it is smaller than the
 623 observed error of our measurements at low TNP-ATP concentrations.

624 **Unroofed binding measurements.**

625 Unroofed membranes were prepared as described previously (*Heuser, 2000; Zagotta
 626 et al., 2016; Puljung et al., 2019*). A coverslip plated with transfected HEK-293T cells was
 627 removed from the culture media and rinsed with PBS. The coverslip was then briefly son-
 628 icated using a probe sonicator (Vibra-cell; Newtown, CT) leaving behind adherent plasma
 629 membrane fragments. Cells cultured on FluoroDishes were rinsed and sonicated directly
 630 in the dish. Unroofed membrane fragments were nearly invisible in bright-field images
 631 and identified by their GFP and ANAP fluorescence. Fluorescent TNP-nucleotides (Jena
 632 Bioscience; Jena, Germany) were diluted in bath solution and perfused onto unroofed
 633 membranes using a valve controlled microvolume superfusion system (μ Flow, ALA Sci-
 634 entific Instruments; Farmingdale, NY).

635 Fluorescence spectra were collected as described above. A region of interest corre-
 636 sponding to the membrane fragment was manually selected and line-averaged for each
 637 wavelength. A similarly sized region of background was selected and averaged, then
 638 subtracted from the spectrum of interest. After subtraction, ANAP intensity was calcu-
 639 lated by averaging the fluorescence intensity measured between 469.5 nm and 474.5 nm.
 640 Bleaching was corrected by fitting the normalised ANAP intensity of exposures taken dur-
 641 ing perfusion with nucleotide-free solution to a single exponential decay of the form

$$\frac{F}{F_{max}} = ae^{kt} + (1 - a) \quad (1)$$

642 then using the fit to correct the intensity of exposures taken during perfusion with test
 643 nucleotide solutions.

644 Some experiments were excluded from further analysis due to obvious cross-contamination
 645 between different solutions within the μ Flow superfusion system. These were identified
 646 by noticeable colour changes in the solution in the delivery tubes.

647 **Patch-clamp fluorometry.**

648 The tip of the patch pipette was centred on the slit of the spectrometer immediately after
 649 patch excision. Currents were measured as described above. Fluorescence emission
 650 spectra from the excised patch were acquired concurrently with current measurements,
 651 both during test solution application as well as nucleotide-free solution. Background
 652 subtraction was slightly imperfect due to the exclusion of TNP-ATP from volume of the
 653 glass of the pipette, resulting in spectra that have negative intensities at the TNP-ATP
 654 peak at high nucleotide concentrations. However, this over-subtraction does not affect
 655 the size of the ANAP peak, which we used to quantify nucleotide binding.

656 ANAP bleaching was corrected as for the unroofed binding experiments with Equa-
 657 tion 1 (Figure 2-Figure supplement 3A). Due to the lower signal-to-noise ratio for PCF
 658 compared to the unroofed membranes, we performed experiments from both high-to-
 659 low and low-to-high TNP-ATP concentrations to minimise artifacts from our bleaching
 660 corrections. Kir6.2*-GFP + SUR1 showed consistent bleaching time courses (Figure 2-
 661 Figure supplement 3B) and an average of 34% of the initial ANAP fluorescence intensity
 662 remained at the end of each experiment (Figure 2-Figure supplement 3C).

663 Some experiments were excluded from further analysis due to low fluorescence in-
 664 tensity, as we were concerned about a low signal to noise ratio influencing our results.

665 **Data processing and presentation.**

666 Raw spectrographic images and current traces were pre-processed in Python and Clamp-
 667 fit (Axon) before analysis with R. Where applicable, all experimental data points are dis-
 668 played in each figure. The number of experiments is reported in the figure legends and
 669 tables. To help visualise uncertainty and prevent some data points being hidden, they are
 670 arranged with a small amount of horizontal jitter; vertical position remains unaffected.
 671 Unless otherwise stated, summary statistics are overlaid as the mean with error bars rep-
 672 resenting the standard error of the mean. Where these error bars are not visible, they
 673 are smaller than the size of the point used for the mean.

674 Hill fits to fluorescence quenching were nonlinear least-squares fits to the following
 675 equation:

$$\frac{y}{y_{max}} = E_{max} + \frac{1 - E_{max}}{1 + 10^{(EC_{50} - [TNPATP]) \cdot h}} \quad (2)$$

676 where y represents normalised fluorescence intensity and EC_{50} and $[TNPATP]$ are \log_{10}
 677 values. Current inhibition data were fit to the same equation but with y representing
 678 normalised current magnitude, IC_{50} instead of EC_{50} , and I_{max} instead of E_{max} .

679 Bayesian model fitting.

680 The MWC-type models considered (Figure 2 and Figure 2—Figure Supplement 2) were
 681 formulated as follows:

$$\frac{F}{F_{max}} = \frac{K_A[TNPATP](1 + K_A[TNPATP])^3 + LDK_A[TNPATP](1 + DK_A[TNPATP])^3}{(1 + K_A[TNPATP])^4 + L(1 + DK_A[TNPATP])^4} \quad (3)$$

$$\frac{\text{open channels}}{\text{total channels}} = \frac{L(1 + DK_A[TNPATP])^4}{(1 + K_A[TNPATP])^4 + L(1 + DK_A[TNPATP])^4} \quad (4)$$

682 When no ligand is present (i.e. when $[TNPATP] = 0$), Equation 4 becomes:

$$\frac{\text{open channels}}{\text{total channels}} = \frac{L}{1 + L} \quad (5)$$

683 We can use this to normalise the predicted changes in the open fraction to an ob-
 684 served change in current as:

$$\frac{I}{I_{max}} = \frac{L(1 + DK_A[TNPATP])^4}{(1 + K_A[TNPATP])^4 + L(1 + DK_A[TNPATP])^4} \cdot \frac{1 + L}{L} \quad (6)$$

685 Two variations on the full MWC model were also considered, and diagrammatic for-
 686 mulations are shown in Figure 2 - Figure supplement 1. The first was similar to the MWC-
 687 type model, except that the channels close after one molecule of TNP-ATP binding with
 688 subsequent binding events having no effect.

$$\frac{F}{F_{max}} = \frac{LDK_A[TNPATP](1 + 3K_A[TNPATP] + 3K_A^2[TNPATP]^2 + K_A^3[TNPATP]^3) + K_A[TNPATP](1 + K_A[TNPATP])^3}{L(1 + 4DK_A[TNPATP] + 6DK_A^2[TNPATP]^2 + 4DK_A^3[TNPATP]^3 + DK_A^4[TNPATP]^4) + (1 + K_A[TNPATP])^4} \quad (7)$$

$$\frac{I}{I_{max}} = \frac{L(1 + 4DK_A[TNPATP] + 6DK_A^2[TNPATP]^2 + 4DK_A^3[TNPATP]^3 + DK_A^4[TNPATP]^4)}{L(1 + 4DK_A[TNPATP] + 6DK_A^2[TNPATP]^2 + 4DK_A^3[TNPATP]^3 + DK_A^4[TNPATP]^4 + (1 + K_A[TNPATP])^4} \cdot \frac{1 + L}{L} \quad (8)$$

689 The second alternate model was the same as the full MWC model, but with an additional term C describing binding cooperativity between Kir6.2 subunits.

$$\frac{F}{F_{max}} = \frac{LDK_A[TNPATP](1 + 3CDK_A[TNPATP] + 3C^2D^2K_A^2[TNPATP]^2 + C^3D^3K_A^3[TNPATP]^3) + K_A[TNPATP](1 + 3CK_A[TNPATP] + 3C^2K_A^2[TNPATP]^2 + C^3K_A^3[TNPATP]^3)}{L(1 + 4DK_A[TNPATP] + 6CD^2K_A^2[TNPATP]^2 + 4C^2D^3K_A^3[TNPATP]^3 + C^3D^4K_A^4[TNPATP]^4) + 1 + 4K_A[TNPATP] + 6CK_A^2[TNPATP]^2 + 4C^2K_A^3[TNPATP]^3 + C^3K_A^4[TNPATP]^4} \quad (9)$$

$$\frac{I}{I_{max}} = \frac{L(1 + 4DK_A[TNPATP] + 6CD^2K_A^2[TNPATP]^2 + 4C^2D^3K_A^3[TNPATP]^3 + C^3D^4K_A^4[TNPATP]^4)}{L(1 + 4DK_A[TNPATP] + 6CD^2K_A^2[TNPATP]^2 + 4C^2D^3K_A^3[TNPATP]^3 + C^3D^4K_A^4[TNPATP]^4 + 1 + 4K_A[TNPATP] + 6CK_A^2[TNPATP]^2 + 4C^2K_A^3[TNPATP]^3 + C^3K_A^4[TNPATP]^4)} \cdot \frac{1 + L}{L} \quad (10)$$

691 Each model was fit to the combined patch-clamp fluorometry datasets using the brms
 692 package (*Gelman et al., 2015; Burkner, 2017*) in R. Prior probability distributions for each
 693 parameter were supplied as:

$$\log_{10}(L) \sim Normal(\mu : 0, \sigma^2 : 0.7)$$

$$D \sim Uniform(min : 0, max : 1)$$

(11)

$$\log_{10}(K_A) \sim Uniform(min : 2, max : 6)$$

$$C \sim Uniform(min : 0, max : 1)$$

694 so that all priors are flat apart from L , which is weakly informative with 99% of its density
 695 falling between unliganded open probabilities of 0.01 and 0.99, and 85% falling between
 696 0.1 and 0.9.

697 We considered two alternative sets of priors for fitting the MWC-type model to our mu-
 698 tant constructs (Figure 4-Figure supplement 4). We generated a narrow informative prior
 699 by fitting normal distributions to the posterior probability density of our fits to Kir6.2*-
 700 GFP + SUR1, and a broad informative prior by increasing the standard deviation of the

701 fitted normal distribution by a factor of ten (Figure 4-Figure supplement 4A). Using nar-
 702 row informative priors results in worse fits as it does not allow for high enough values
 703 of D to explain the data, whereas the broad informative priors result in fits which do not
 704 visibly differ much from the neutral priors (Figure 4-Figure supplement 4B). Whereas the
 705 fits using the broad informative priors were visually similar to those using neutral priors,
 706 the posterior probability distributions for the parameters were slightly different (Figure
 707 4-Figure supplement 4C). Notably, due to the broad prior distribution supplied for L , the
 708 posterior probability distribution for L is also very broad for each construct, with a large
 709 amount of probability density over unlikely values, i.e. over half the probability density
 710 for Kir6.2*-GFP + SUR1-K205A and Kir6.2*-GFP + SUR1-K205E is for L values lower than
 711 0.01 (corresponding to a biologically implausible unliganded $P_{open} < 0.01$).

712 Each model was run with 4 independent chains for 10,000 iterations each after a burn-
 713 in period of 20,000 iterations, saving every 10th sample for a total of 4,000 samples per
 714 model. Each model parameter achieved a minimum effective sample size of 3,500 and
 715 a potential scale reduction statistic (\hat{R}) of 1.00. Where applicable, the posterior proba-
 716 bilities of each parameter are reported as the median and the 95% equal-tailed interval.
 717 Bayes factors were calculated using bridge-sampling (*Gronau et al., 2017*), and leave-one-
 718 out cross-validation (LOO-CV) was performed using the loo package (*Vehtari et al., 2017*).

719 Docking.

720 Computational docking of TNP-ATP into the nucleotide binding site of Kir6.2 was per-
 721 formed using AutoDock-Vina (*Trott and Olson, 2010*) and Pymol (Schrödinger, LLC; New
 722 York, NY). 11 TNP-ATP structures from the Protein Data Bank (PDB accession #s 1I5D,
 723 3AR7, 5NCQ, 5SVQ, 5XW6, 2GVD, 5A3S, 2PMK, and 3B5J) were used as starting poses and
 724 a 15x11.25x15 Å box was centred on the ATP bound to Kir6.2 in PDB accession #6BAA
 725 (*Martin et al., 2017*). Protonation states for each residue were assigned using PDB2PQR
 726 and PROPKA 3.0 (*Dolinsky et al., 2004*). The modal highest-scoring pose from the dock-
 727 ing run was selected (PDB accession #5XW6, *Kasuya et al. (2017)*) and distances were

728 measured from a pseudo atom at the centre of the fluorescent moiety. TNP-ATP (PDB
 729 #3AR7, *Toyoshima et al. (2011)*) was positioned into the first nucleotide binding domain
 730 of SUR1 (PDB #6PZI, *Martin et al. (2019)*) using the alignment tool in Pymol.

731 **Chemicals and stock solutions.**

732 Unless otherwise noted, all chemicals were obtained from Sigma. TNP-ATP was obtained
 733 as a 10 mM aqueous stock from Jena Bioscience and stored at –20 °C. 1 mM aqueous
 734 stocks of ANAP-TFA were prepared by dissolving the free acid in 30 mM NaOH, and were
 735 stored at –20 °C. Tolbutamide stocks (50 mM) were prepared in 100 mM KOH and stored
 736 at –20 °C.

737 **Data availability**

738 All data sets and the code used to analyse and present them are available on GitHub at
 739 https://github.com/smusher/KATP_paper_2019 and have also been uploaded to Dryad
 740 at <https://doi.org/10.5061/dryad.0vt4b8gtr>.

741 **Acknowledgments**

742 We wish to thank Raul Terron Exposito for technical assistance and Dr. Natascia Vedovato
 743 for helpful discussions. Dr. James Cantley provided access to the Licor scanner for west-
 744 ern blots. This work was supported by the Biotechnology and Biological Science Research
 745 Council (BB/R002517/1) and the Wellcome Trust Oxion graduate program.

746 **References**

- 747 **Aguilar-Bryan L**, Nichols CG, Wechsler SW, Clement JP, Boyd r A E, Gonzalez G, Herrera-Sosa H,
 748 Nguy K, Bryan J, Nelson DA. Cloning of the beta cell high-affinity sulfonylurea receptor: a regu-
 749 lator of insulin secretion. *Science*. 1995; 268(5209):423–6. <https://www.ncbi.nlm.nih.gov/pubmed/7716547>.
- 750
- 751 **Ashcroft FM**, Puljung MC, Vedovato N. Neonatal Diabetes and the KATP Channel: From Mutation to

- 752 Therapy. Trends Endocrinol Metab. 2017; 28(5):377–387. <https://www.ncbi.nlm.nih.gov/pubmed/28262438>, doi: 10.1016/j.tem.2017.02.003.
- 754 **Ashcroft FM**, Rorsman P. K(ATP) channels and islet hormone secretion: new insights and contro-
755 versies. Nat Rev Endocrinol. 2013; 9(11):660–9. <https://www.ncbi.nlm.nih.gov/pubmed/24042324>,
756 doi: 10.1038/nrendo.2013.166.
- 757 **Babenko AP**, Bryan J. Sur domains that associate with and gate KATP pores define a novel gate-
758 keeper. J Biol Chem. 2003; 278(43):41577–80. <https://www.ncbi.nlm.nih.gov/pubmed/12941953>,
759 doi: 10.1074/jbc.C300363200.
- 760 **Biskup C**, Kusch J, Schulz E, Nache V, Schwede F, Lehmann F, Hagen V, Benndorf K. Relating ligand
761 binding to activation gating in CNGA2 channels. Nature. 2007; 446(7134):440–3. <https://www.ncbi.nlm.nih.gov/pubmed/17322905>, doi: 10.1038/nature05596.
- 763 **Burkner PC**. brms: An R Package for Bayesian Multilevel Models Using Stan. Journal of Statistical
764 Software. 2017; 80(1):1–28. <GotolSI>:/WOS:000408409900001.
- 765 **Chan KW**, Zhang H, Logothetis DE. N-terminal transmembrane domain of the SUR controls traf-
766 ficking and gating of Kir6 channel subunits. EMBO J. 2003; 22(15):3833–43. <https://www.ncbi.nlm.nih.gov/pubmed/12881418>, doi: 10.1093/emboj/cdg376.
- 768 **Changeux JP**, Edelstein S. Conformational selection or induced fit? 50 years of debate resolved.
769 F1000 biology reports. 2011; 3.
- 770 **Chatterjee A**, Guo J, Lee HS, Schultz PG. A genetically encoded fluorescent probe in mammalian
771 cells. J Am Chem Soc. 2013; 135(34):12540–3. <https://www.ncbi.nlm.nih.gov/pubmed/23924161>,
772 doi: 10.1021/ja4059553.
- 773 **Corry B**, Jayatilaka D, Rigby P. A flexible approach to the calculation of resonance energy transfer
774 efficiency between multiple donors and acceptors in complex geometries. Biophysical journal.
775 2005; 89(6):3822–3836.
- 776 **Craig TJ**, Ashcroft FM, Proks P. How ATP inhibits the open K(ATP) channel. J Gen Physiol. 2008;
777 132(1):131–44. <https://www.ncbi.nlm.nih.gov/pubmed/18591420>, doi: 10.1085/jgp.200709874.
- 778 **Deplazes E**, Jayatilaka D, Corry B. ExiFRET: flexible tool for understanding FRET in complex geome-
779 tries. Journal of biomedical optics. 2012; 17(1):011005.

- 780 **Ding D**, Wang M, Wu JX, Kang Y, Chen L. The Structural Basis for the Binding of Repaglinide to
781 the Pancreatic KATP Channel. *Cell Rep.* 2019; 27(6):1848–1857 e4. <https://www.ncbi.nlm.nih.gov/pubmed/31067468>, doi: 10.1016/j.celrep.2019.04.050.
- 783 **Dolinsky TJ**, Nielsen JE, McCammon JA, Baker NA. PDB2PQR: an automated pipeline for the
784 setup of Poisson-Boltzmann electrostatics calculations. *Nucleic Acids Res.* 2004; 32(Web Server
785 issue):W665–7. <https://www.ncbi.nlm.nih.gov/pubmed/15215472>, doi: 10.1093/nar/gkh381.
- 786 **Drain P**, Geng X, Li L. Concerted gating mechanism underlying KATP channel inhibition by ATP. *Bio-
787 phys J.* 2004; 86(4):2101–12. <https://www.ncbi.nlm.nih.gov/pubmed/15041650>, doi: 10.1016/S0006-
788 3495(04)74269-1.
- 789 **Drain P**, Li L, Wang J. KATP channel inhibition by ATP requires distinct functional domains of the cy-
790 toplasmic C terminus of the pore-forming subunit. *Proc Natl Acad Sci U S A.* 1998; 95(23):13953–8.
791 <https://www.ncbi.nlm.nih.gov/pubmed/9811907>.
- 792 **Enkvetachakul D**, Loussouarn G, Makhina E, Nichols C. ATP interaction with the open state of the
793 KATP channel. *Biophysical Journal.* 2001; 80(2):719–728.
- 794 **Enkvetachakul D**, Loussouarn G, Makhina E, Shyng SL, Nichols CG. The kinetic and physical basis of
795 K(ATP) channel gating: toward a unified molecular understanding. *Biophys J.* 2000; 78(5):2334–
796 48. <https://www.ncbi.nlm.nih.gov/pubmed/10777731>, doi: 10.1016/S0006-3495(00)76779-8.
- 797 **Enkvetachakul D**, Nichols CG. Gating mechanism of KATP channels: function fits form.
798 *J Gen Physiol.* 2003; 122(5):471–80. <https://www.ncbi.nlm.nih.gov/pubmed/14581579>, doi:
799 10.1085/jgp.200308878.
- 800 **Fang K**, Csanady L, Chan KW. The N-terminal transmembrane domain (TMD0) and a cytosolic
801 linker (L0) of sulphonylurea receptor define the unique intrinsic gating of KATP channels. *J Phys-
802 iol.* 2006; 576(Pt 2):379–89. <https://www.ncbi.nlm.nih.gov/pubmed/16887879>, doi: 10.1111/jphysiol.2006.112748.
- 804 **Flanagan SE**, Edghill EL, Gloyn AL, Ellard S, Hattersley AT. Mutations in KCNJ11, which encodes
805 Kir6.2, are a common cause of diabetes diagnosed in the first 6 months of life, with the pheno-
806 type determined by genotype. *Diabetologia.* 2006; 49(6):1190–7. <https://www.ncbi.nlm.nih.gov/pubmed/16609879>, doi: 10.1007/s00125-006-0246-z.

- 808 **Gelman A**, Lee D, Guo JQ. Stan: A Probabilistic Programming Language for Bayesian Inference and
 809 Optimization. *Journal of Educational and Behavioral Statistics*. 2015; 40(5):530–543. <[Go to ISI](#)>:
 810 [//WOS:000363883900006](https://doi.org/10.1080/10709910.2015.1019070).
- 811 **Gloyn AL**, Diatloff-Zito C, Edghill EL, Bellanne-Chantelot C, Nivot S, Coutant R, Ellard S, Hattersley AT,
 812 Robert JJ. KCNJ11 activating mutations are associated with developmental delay, epilepsy and
 813 neonatal diabetes syndrome and other neurological features. *Eur J Hum Genet*. 2006; 14(7):824–
 814 30. <https://www.ncbi.nlm.nih.gov/pmc/articles/PMC16670688/>, doi: 10.1038/sj.ejhg.5201629.
- 815 **Gribble FM**, Tucker SJ, Haug T, Ashcroft FM. MgATP activates the beta cell KATP channel by
 816 interaction with its SUR1 subunit. *Proc Natl Acad Sci U S A*. 1998; 95(12):7185–90. <https://doi.org/10.1073/pnas.95.12.7185>.
 817 [//www.ncbi.nlm.nih.gov/pmc/articles/PMC16670688/](https://www.ncbi.nlm.nih.gov/pmc/articles/PMC16670688/), doi: 10.1073/pnas.95.12.7185.
- 818 **Gronau QF**, Singmann H, Wagenmakers EJ. bridgesampling: An R Package for Estimating Normal-
 819 izing Constants. *arXiv e-prints*. 2017 Oct; p. arXiv:1710.08162.
- 820 **Heuser J**. The production of 'cell cortices' for light and electron microscopy. *Traffic*. 2000; 1(7):545–
 821 52. <https://www.ncbi.nlm.nih.gov/pmc/articles/PMC16670688/>, doi: 10.1085/jgp.201311116.
- 822 **Hines KE**, Middendorf TR, Aldrich RW. Determination of parameter identifiability in nonlinear bio-
 823 physical models: A Bayesian approach. *J Gen Physiol*. 2014; 143(3):401–16. <https://www.ncbi.nlm.nih.gov/pmc/articles/PMC4111116/>, doi: 10.1085/jgp.201311116.
- 824 **Inagaki N**, Gono T, Clement JP, Namba N, Inazawa J, Gonzalez G, Aguilar-Bryan L, Seino S, Bryan
 825 J. Reconstitution of IKATP: an inward rectifier subunit plus the sulfonylurea receptor. *Science*.
 826 1995; 270(5239):1166–70. <https://www.ncbi.nlm.nih.gov/pmc/articles/PMC16670688/>, doi: 10.1126/science.270.5239.1166.
- 827 **Inagaki N**, Gono T, Seino S. Subunit stoichiometry of the pancreatic beta-cell ATP-sensitive K+
 828 channel. *FEBS Lett*. 1997; 409(2):232–6. <https://www.ncbi.nlm.nih.gov/pmc/articles/PMC16670688/>, doi: 10.1016/S0014-5793(97)80032-2.
- 829 **John SA**, Monck JR, Weiss JN, Ribalet B. The sulphonylurea receptor SUR1 regulates ATP-sensitive
 830 mouse Kir6.2 K+ channels linked to the green fluorescent protein in human embryonic kidney
 831 cells (HEK 293). *J Physiol*. 1998; 510 (Pt 2):333–45. <https://www.ncbi.nlm.nih.gov/pmc/articles/PMC16670688/>, doi: 10.1111/j.1469-7793.1998.333bk.x.
- 832 **Kasuya G**, Yamaura T, Ma XB, Nakamura R, Takemoto M, Nagumo H, Tanaka E, Dohmae N, Nakane
 833 T, Yu Y, Ishitani R, Matsuzaki O, Hattori M, Nureki O. Structural insights into the competitive

- 836 inhibition of the ATP-gated P2X receptor channel. *Nat Commun.* 2017; 8(1):876. <https://www.ncbi.nlm.nih.gov/pubmed/29026074>, doi: 10.1038/s41467-017-00887-9.
- 837
- 838 **Kusch J**, Biskup C, Thon S, Schulz E, Nache V, Zimmer T, Schwede F, Benndorf K. Interdependence of
839 receptor activation and ligand binding in HCN2 pacemaker channels. *Neuron.* 2010; 67(1):75–85.
840 <https://www.ncbi.nlm.nih.gov/pubmed/20624593>, doi: 10.1016/j.neuron.2010.05.022.
- 841 **Li L**, Wang J, Drain P. The I182 region of k(ir)6.2 is closely associated with ligand binding in K(ATP)
842 channel inhibition by ATP. *Biophys J.* 2000; 79(2):841–52. <https://www.ncbi.nlm.nih.gov/pubmed/10920016>, doi: 10.1016/S0006-3495(00)76340-5.
- 843
- 844 **Lin CY**, Huang Z, Wen W, Wu A, Wang C, Niu L. Enhancing Protein Expression in HEK-293 Cells by
845 Lowering Culture Temperature. *PLoS One.* 2015; 10(4):e0123562. <https://www.ncbi.nlm.nih.gov/pubmed/25893827>, doi: 10.1371/journal.pone.0123562.
- 846
- 847 **Makhina EN**, Nichols CG. Independent trafficking of KATP channel subunits to the plasma mem-
brane. *J Biol Chem.* 1998; 273(6):3369–74. <https://www.ncbi.nlm.nih.gov/pubmed/9452456>.
- 848
- 849 **Markworth E**, Schwanstecher C, Schwanstecher M. ATP4- mediates closure of pancreatic beta-
850 cell ATP-sensitive potassium channels by interaction with 1 of 4 identical sites. *Diabetes.* 2000;
851 49(9):1413–8. <https://www.ncbi.nlm.nih.gov/pubmed/10969823>, doi: 10.2337/diabetes.49.9.1413.
- 852
- 853 **Martin GM**, Kandasamy B, DiMaio F, Yoshioka C, Shyng SL. Anti-diabetic drug binding site in a
mammalian KATP channel revealed by Cryo-EM. *Elife.* 2017; 6. <https://www.ncbi.nlm.nih.gov/pubmed/29035201>, doi: 10.7554/eLife.31054.
- 854
- 855 **Martin GM**, Sung MW, Yang Z, Innes LM, Kandasamy B, David LL, Yoshioka C, Shyng SL. Mechanism
856 of pharmacochaperoning in a mammalian KATP channel revealed by cryo-EM. *Elife.* 2019; 8.
857 <https://www.ncbi.nlm.nih.gov/pubmed/31343405>, doi: 10.7554/eLife.46417.
- 858
- 859 **Masia R**, Koster JC, Tumini S, Chiarelli F, Colombo C, Nichols CG, Barbetti F. An ATP-binding mu-
tation (G334D) in KCNJ11 is associated with a sulfonylurea-insensitive form of developmental
860 delay, epilepsy, and neonatal diabetes. *Diabetes.* 2007; 56(2):328–36. <https://www.ncbi.nlm.nih.gov/pubmed/17259376>, doi: 10.2337/db06-1275.
- 861
- 862 **McTaggart JS**, Clark RH, Ashcroft FM. The role of the KATP channel in glucose homeostasis in

- 863 health and disease: more than meets the islet. *J Physiol.* 2010; 588(Pt 17):3201–9. <https://www.ncbi.nlm.nih.gov/pubmed/20519313>, doi: 10.1113/jphysiol.2010.191767.
- 864
- 865 **Monod J**, Wyman J, Changeux JP. On the Nature of Allosteric Transitions: A Plausible Model. *J Mol Biol.* 1965; 12:88–118. <https://www.ncbi.nlm.nih.gov/pubmed/14343300>.
- 866
- 867 **Nichols CG**, Shyng SL, Nestorowicz A, Glaser B, Clement JP, Gonzalez G, Aguilar-Bryan L, Permutt MA, Bryan J. Adenosine diphosphate as an intracellular regulator of insulin secretion. *Science.* 1996; 272(5269):1785–7. <https://www.ncbi.nlm.nih.gov/pubmed/8650576>.
- 868
- 869
- 870 **Pratt EB**, Zhou Q, Gay JW, Shyng SL. Engineered interaction between SUR1 and Kir6.2 that enhances ATP sensitivity in KATP channels. *J Gen Physiol.* 2012; 140(2):175–87. <https://www.ncbi.nlm.nih.gov/pubmed/22802363>, doi: 10.1085/jgp.201210803.
- 871
- 872
- 873 **Proks P**, Puljung MC, Vedovato N, Sachse G, Mulvaney R, Ashcroft FM. Running out of time: the decline of channel activity and nucleotide activation in adenosine triphosphate-sensitive K⁺ channels. *Philos Trans R Soc Lond B Biol Sci.* 2016; 371(1700). <https://www.ncbi.nlm.nih.gov/pubmed/27377720>, doi: 10.1098/rstb.2015.0426.
- 874
- 875
- 876
- 877 **Proks P**, de Wet H, Ashcroft FM. Activation of the K(ATP) channel by Mg-nucleotide interaction with SUR1. *J Gen Physiol.* 2010; 136(4):389–405. <https://www.ncbi.nlm.nih.gov/pubmed/20876358>, doi: 10.1085/jgp.201010475.
- 878
- 879
- 880 **Puljung M**, Vedovato N, Usher S, Ashcroft F. Activation mechanism of ATP-sensitive K(+) channels explored with real-time nucleotide binding. *Elife.* 2019; 8. <https://www.ncbi.nlm.nih.gov/pubmed/30789344>, doi: 10.7554/eLife.41103.
- 881
- 882
- 883 **Puljung MC**. Cryo-electron microscopy structures and progress toward a dynamic understanding of KATP channels. *J Gen Physiol.* 2018; 150(5):653–669. <https://www.ncbi.nlm.nih.gov/pubmed/29685928>, doi: 10.1085/jgp.201711978.
- 884
- 885
- 886 **Quan Y**, Barszczuk A, Feng ZP, Sun HS. Current understanding of K ATP channels in neonatal diseases: focus on insulin secretion disorders. *Acta Pharmacol Sin.* 2011; 32(6):765–80. <https://www.ncbi.nlm.nih.gov/pubmed/21602835>, doi: 10.1038/aps.2011.57.
- 887
- 888
- 889 **Ribalet B**, John SA, Xie LH, Weiss JN. ATP-sensitive K⁺ channels: regulation of bursting by the

- 890 sulphonylurea receptor, PIP2 and regions of Kir6.2. *J Physiol.* 2006; 571(Pt 2):303–17. <https://www.ncbi.nlm.nih.gov/pubmed/16373383>, doi: 10.1113/jphysiol.2005.100719.
- 891
- 892 **Sakura H**, Ammala C, Smith PA, Gribble FM, Ashcroft FM. Cloning and functional expression of the
893 cDNA encoding a novel ATP-sensitive potassium channel subunit expressed in pancreatic beta-
894 cells, brain, heart and skeletal muscle. *FEBS Lett.* 1995; 377(3):338–44. <https://www.ncbi.nlm.nih.gov/pubmed/8549751>, doi: 10.1016/0014-5793(95)01369-5.
- 895
- 896 **Schmied WH**, Elsasser SJ, Uttamapinant C, Chin JW. Efficient multisite unnatural amino acid incor-
897 poration in mammalian cells via optimized pyrrolysyl tRNA synthetase/tRNA expression and en-
898 gineered eRF1. *J Am Chem Soc.* 2014; 136(44):15577–83. <https://www.ncbi.nlm.nih.gov/pubmed/25350841>, doi: 10.1021/ja5069728.
- 899
- 900 **Snider KE**, Becker S, Boyajian L, Shyng SL, MacMullen C, Hughes N, Ganapathy K, Bhatti T, Stanley
901 CA, Ganguly A. Genotype and phenotype correlations in 417 children with congenital hyperin-
902 sulinism. *J Clin Endocrinol Metab.* 2013; 98(2):E355–63. <https://www.ncbi.nlm.nih.gov/pubmed/23275527>, doi: 10.1210/jc.2012-2169.
- 903
- 904 **Toyoshima C**, Yonekura S, Tsueda J, Iwasawa S. Trinitrophenyl derivatives bind differently from par-
905 ent adenine nucleotides to Ca²⁺-ATPase in the absence of Ca²⁺. *Proc Natl Acad Sci U S A.* 2011;
906 108(5):1833–8. <https://www.ncbi.nlm.nih.gov/pubmed/21239683>, doi: 10.1073/pnas.1017659108.
- 907
- 908 **Trapp S**, Proks P, Tucker SJ, Ashcroft FM. Molecular analysis of ATP-sensitive K channel gating and
909 implications for channel inhibition by ATP. *J Gen Physiol.* 1998; 112(3):333–49. <https://www.ncbi.nlm.nih.gov/pubmed/9725893>, doi: 10.1085/jgp.112.3.333.
- 910
- 911 **Trott O**, Olson AJ. AutoDock Vina: improving the speed and accuracy of docking with a new scoring
912 function, efficient optimization, and multithreading. *J Comput Chem.* 2010 Jan; 31(2):455–461.
- 913
- 914 **Tucker SJ**, Gribble FM, Zhao C, Trapp S, Ashcroft FM. Truncation of Kir6.2 produces ATP-sensitive
915 K⁺ channels in the absence of the sulphonylurea receptor. *Nature.* 1997; 387(6629):179–83.
<https://www.ncbi.nlm.nih.gov/pubmed/9144288>, doi: 10.1038/387179a0.
- 916
- 917 **Tusnady GE**, Bakos E, Varadi A, Sarkadi B. Membrane topology distinguishes a subfamily of the
918 ATP-binding cassette (ABC) transporters. *FEBS Lett.* 1997; 402(1):1–3. <https://www.ncbi.nlm.nih.gov/pubmed/9013845>, doi: 10.1016/s0014-5793(96)01478-0.

- 918 **Ueda K**, Komine J, Matsuo M, Seino S, Amachi T. Cooperative binding of ATP and MgADP in the
919 sulfonylurea receptor is modulated by glibenclamide. *Proc Natl Acad Sci U S A*. 1999; 96(4):1268–
920 72. <https://www.ncbi.nlm.nih.gov/pubmed/9990013>.
- 921 **Vedovato N**, Ashcroft FM, Puljung MC. The Nucleotide-Binding Sites of SUR1: A Mechanistic
922 Model. *Biophys J*. 2015; 109(12):2452–60. <https://www.ncbi.nlm.nih.gov/pubmed/26682803>, doi:
923 10.1016/j.bpj.2015.10.026.
- 924 **Vehtari A**, Gelman A, Gabry J. Practical Bayesian model evaluation using leave-one-out cross-
925 validation and WAIC (vol 27, pg 1413, 2017). *Statistics and Computing*. 2017; 27(5):1433–1433.
926 <GotolSI>://WOS:000400831700018, doi: 10.1007/s11222-016-9709-3.
- 927 **Wagenmakers EJ**. A practical solution to the pervasive problems of p values. *Psychon Bull Rev*.
928 2007; 14(5):779–804. <https://www.ncbi.nlm.nih.gov/pubmed/18087943>.
- 929 **Wang R**, Zhang X, Cui N, Wu J, Piao H, Wang X, Su J, Jiang C. Subunit-stoichiometric evidence
930 for kir6.2 channel gating, ATP binding, and binding-gating coupling. *Mol Pharmacol*. 2007;
931 71(6):1646–56. <https://www.ncbi.nlm.nih.gov/pubmed/17369308>, doi: 10.1124/mol.106.030528.
- 932 **Wu S**, Vysotskaya ZV, Xu X, Xie C, Liu Q, Zhou L. State-dependent cAMP binding to functioning HCN
933 channels studied by patch-clamp fluorometry. *Biophys J*. 2011; 100(5):1226–32. <https://www.ncbi.nlm.nih.gov/pubmed/21354395>, doi: 10.1016/j.bpj.2011.01.034.
- 935 **Yan FF**, Lin YW, MacMullen C, Ganguly A, Stanley CA, Shyng SL. Congenital hyperinsulinism asso-
936 ciated ABCC8 mutations that cause defective trafficking of ATP-sensitive K⁺ channels: identifica-
937 tion and rescue. *Diabetes*. 2007; 56(9):2339–48. <https://www.ncbi.nlm.nih.gov/pubmed/17575084>,
938 doi: 10.2337/db07-0150.
- 939 **Zagotta WN**, Gordon MT, Senning EN, Munari MA, Gordon SE. Measuring distances between
940 TRPV1 and the plasma membrane using a noncanonical amino acid and transition metal ion
941 FRET. *J Gen Physiol*. 2016; 147(2):201–16. <https://www.ncbi.nlm.nih.gov/pubmed/26755770>, doi:
942 10.1085/jgp.201511531.
- 943 **Zerangue N**, Schwappach B, Jan YN, Jan LY. A new ER trafficking signal regulates the subunit sto-
944 chiometry of plasma membrane K(ATP) channels. *Neuron*. 1999; 22(3):537–48. <https://www.ncbi.nlm.nih.gov/pubmed/10197533>.

946 **Zheng J, Zagotta WN.** Patch-clamp fluorometry recording of conformational rearrangements of
947 ion channels. *Sci STKE*. 2003; 2003(176):PL7. <https://www.ncbi.nlm.nih.gov/pubmed/12671191>, doi:
948 [10.1126/stke.2003.176.pl7](https://doi.org/10.1126/stke.2003.176.pl7).

949 **Tables and supplementary figures**

Fluorescence Quenching	Construct	Term	Estimate	Standard Error
<i>TNP-ATP</i>	Kir6.2*-GFP+SUR1 n = 18	EC_{50}	-4.59 (25.7)	0.05
		h	0.82	0.05
		E_{max}	0.93	0.03
	Kir6.2*,G334D-GFP+SUR1 n = 9	EC_{50}	-3.31 (490)	2.23
		h	2.63	17.70
		E_{max}	0.08	0.26
	Kir6.2*,C166S-GFP+SUR1 n = 12	EC_{50}	-4.50 (31.6)	0.05
		h	0.92	0.08
		E_{max}	0.87	0.03
	Kir6.2*-GFP n = 14	EC_{50}	-4.42 (38.0)	0.05
		h	0.83	0.05
		E_{max}	0.92	0.03

Table 1. Table 1: Hill fit parameters from unroofed membranes. EC_{50} values and their standard errors are reported as $\log_{10} M$. EC_{50} values are also provided as μM in parenthesis.

Current Inhibition	Construct	Term	Estimate	Standard Error
<i>ATP</i>	Kir6.2-GFP+SUR1 n = 3	IC_{50}	-4.20 (63.1)	0.07
		h	1.28	0.21
		I_{max}	0.99	0.06
	Kir6.2-GFP n = 2	IC_{50}	-3.31 (490)	0.05
		h	1.15	0.12
		I_{max}	0.93	0.03
	Kir6.2*-GFP+SUR1 n = 4	IC_{50}	-4.10 (79.4)	0.06
		h	1.42	0.21
		I_{max}	1.00	0.05
<i>TNP-ATP</i>	Kir6.2-GFP+SUR1 n = 7	IC_{50}	-5.93 (1.17)	0.04
		h	1.14	0.11
		I_{max}	0.97	0.02
	Kir6.2-GFP n = 3	IC_{50}	-3.56 (275)	0.64
		h	1.09	0.85
		I_{max}	1.00	0.53
	Kir6.2*-GFP+SUR1 n = 9	IC_{50}	-5.21 (6.17)	0.10
		h	0.92	0.18
		I_{max}	0.96	0.05
	Kir6.2*,C166S-GFP+SUR1 n = 6	IC_{50}	-3.11 (776)	0.23
		h	1.35	1.16
		I_{max}	0.55	0.11
	Kir6.2*-GFP+SUR-K205A n = 9	IC_{50}	-3.78 (166)	0.45
		h	0.75	0.30
		I_{max}	1.00	0.29
	Kir6.2*-GFP+SUR-K205E n = 9	IC_{50}	-3.20 (631)	2.15
		h	0.79	0.84
		I_{max}	1.00	1.77
Fluorescence Quenching				
<i>TNP-ATP</i>	Kir6.2*-GFP+SUR1 n = 9	EC_{50}	-4.11 (77.6)	0.09
		h	0.87	0.11
		E_{max}	1.00	0.06
	Kir6.2*,C166S-GFP+SUR1 n = 6	EC_{50}	-4.17 (67.6)	0.23
		h	0.84	0.27
		E_{max}	1.00	0.14
	Kir6.2*-GFP+SUR-K205A n = 9	EC_{50}	-3.69 (204)	0.42
		h	0.73	0.25
		E_{max}	1.00	0.27
	Kir6.2*-GFP+SUR-K205E n = 9	EC_{50}	-3.37 (427)	1.10
		h	0.74	0.47
		E_{max}	1.00	0.79

Table 2. Table 2: Hill fit parameters from excised patches. EC_{50} and IC_{50} values and their standard errors are reported as $\log_{10} M$. EC_{50} and IC_{50} values are also provided as μM in parenthesis.

Full MWC		Term	Estimate	2.5% Quantile	97.5% Quantile
Kir6.2*-GFP+SUR1 n = 9	<i>L</i>	-1.05	-1.85	-0.45	
	<i>D</i>	0.04	0.00	0.19	
	<i>K_A</i>	4.32	4.21	4.44	
Kir6.2*,C166S-GFP+SUR1 n = 6	<i>L</i>	0.29	-1.04	1.41	
	<i>D</i>	0.84	0.52	0.95	
	<i>K_A</i>	4.18	3.93	4.47	
Kir6.2*-GFP+SUR-K205A n = 9	<i>L</i>	-0.37	-1.34	0.41	
	<i>D</i>	0.55	0.39	0.65	
	<i>K_A</i>	3.76	3.59	3.95	
Kir6.2*-GFP+SUR-K205E n = 9	<i>L</i>	-0.18	-1.25	0.70	
	<i>D</i>	0.62	0.42	0.74	
	<i>K_A</i>	3.40	3.21	3.62	
Single-site					
Kir6.2*-GFP+SUR1 n = 9	<i>L</i>	-1.06	-1.84	-0.47	
	<i>D</i>	0.05	0.01	0.10	
	<i>K_A</i>	4.33	4.22	4.44	
Kir6.2*,C166S-GFP+SUR1 n = 6	<i>L</i>	0.09	-1.15	1.05	
	<i>D</i>	0.70	0.29	0.91	
	<i>K_A</i>	4.15	3.88	4.43	
Kir6.2*-GFP+SUR-K205A n = 9	<i>L</i>	-0.25	-1.30	0.53	
	<i>D</i>	0.18	0.06	0.32	
	<i>K_A</i>	3.62	3.45	3.83	
Kir6.2*-GFP+SUR-K205E n = 9	<i>L</i>	-0.19	-1.19	0.52	
	<i>D</i>	0.30	0.13	0.47	
	<i>K_A</i>	3.31	3.13	3.50	
Negative cooperativity					
Kir6.2*-GFP+SUR1 n = 9	<i>L</i>	-0.42	-1.38	0.48	
	<i>D</i>	0.15	0.02	0.29	
	<i>K_A</i>	4.82	4.54	5.29	
	<i>C</i>	0.17	0.06	0.36	
Kir6.2*,C166S-GFP+SUR1 n = 6	<i>L</i>	0.32	-0.96	1.47	
	<i>D</i>	0.83	0.50	0.94	
	<i>K_A</i>	4.43	4.04	5.14	
	<i>C</i>	0.52	0.09	0.97	
Kir6.2*-GFP+SUR-K205A n = 9	<i>L</i>	-0.16	-1.18	0.64	
	<i>D</i>	0.52	0.32	0.64	
	<i>K_A</i>	4.10	3.73	4.68	
	<i>C</i>	0.35	0.10	0.91	
Kir6.2*-GFP+SUR-K205E n = 9	<i>L</i>	0.03	-1.11	0.99	
	<i>D</i>	0.58	0.32	0.73	
	<i>K_A</i>	3.71	3.34	4.41	
	<i>C</i>	0.45	0.10	0.96	

Table 3. Table 3: Fitted parameters for the MWC-type models. *L*, *K_A* and their associated quantiles are reported as log₁₀ values to maintain consistency of the accuracy they are reported at.

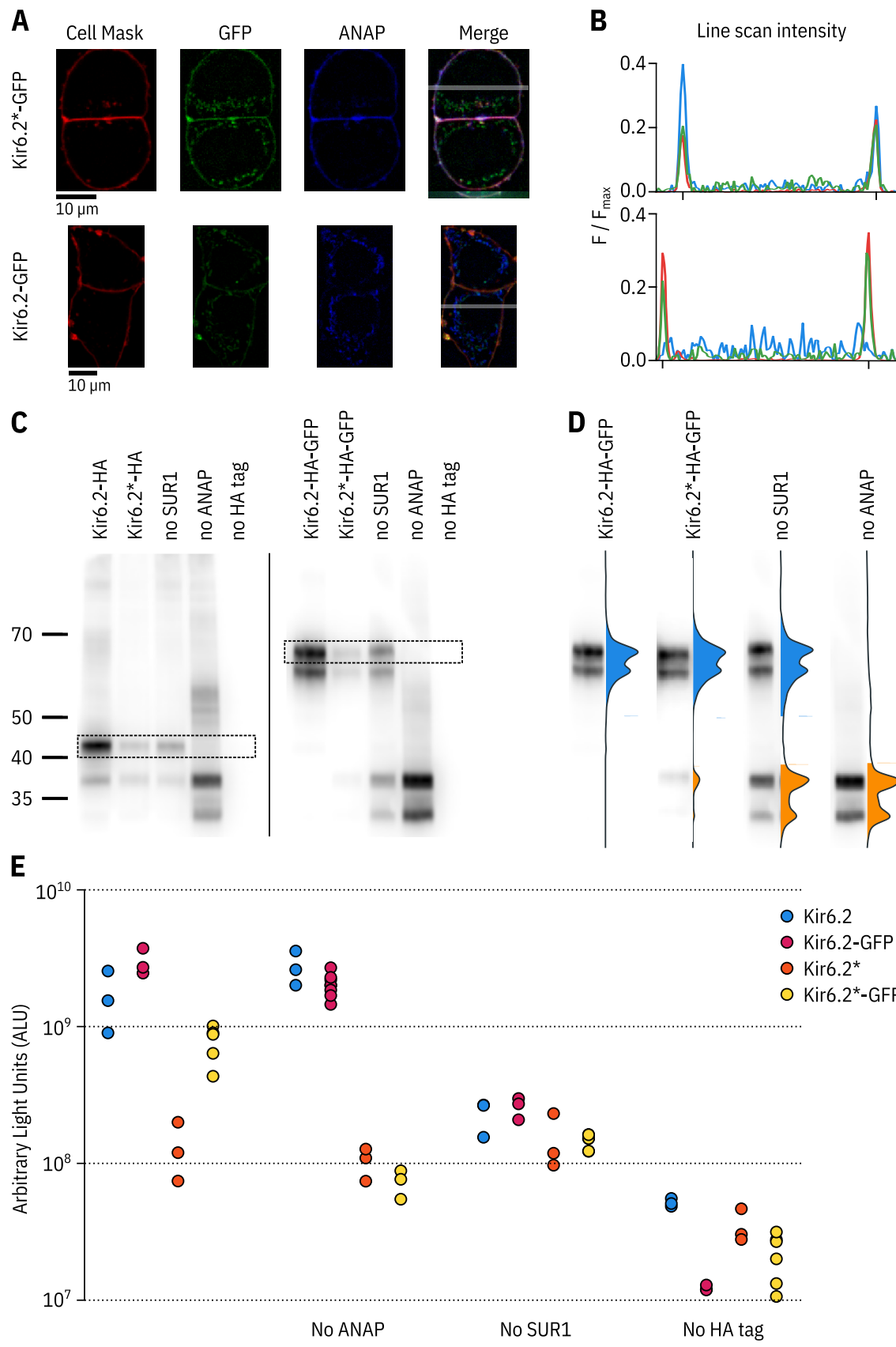


Figure 1 – figure supplement 1. ANAP labelling is specific and only full-length Kir6.2 is expressed at the cell membrane.

Figure 1 – figure supplement 1. ANAP labelling is specific and only full-length Kir6.2 is expressed at the cell membrane.

A. Confocal images of HEK-293T cells transfected with Kir6.2*-GFP + SUR1 (top panel) or Kir6.2-GFP + SUR1 (bottom panel). Cells were stained with Cell Mask Deep Red to label the plasma membrane. The grey band in the merged image is a 5-pixel width line scan. **B.** Averaged intensities of the line scans shown in **A**. The intensity of each channel is shown as a differently coloured line: Cell Mask in red, ANAP in blue and GFP in green. The notches on the x-axis mark the location of the plasma membrane. **C.** Two separate western blots against Kir6.2*-HA (left) and Kir6.2*-HA-GFP (right) constructs. The HA tag is in the extracellular region following helix M1 of Kir6.2, and is present in constructs in **C**, **D**, and **E** unless otherwise stated. Cells were co-transfected with pANAP, eRF1-E55D, and SUR1 unless otherwise indicated. Full-length Kir6.2 constructs are indicated on each gel with a dashed box. The doublets represent an N-terminally truncated product - see Materials and Methods. **D.** Each lane from the Kir6.2*-HA-GFP gel is displayed normalised to its highest intensity accompanied by the line averaged density trace. The density peak corresponding to ANAP-labelled Kir6.2 is filled in blue. The density peak for C-terminally truncated Kir6.2 is filled in orange. **E.** Chemiluminescence-based surface expression assay for Kir6.2-HA constructs. Each data point represents an individual coverslip of transfected HEK-293T cells. n = 3-6 for each condition. Note the logarithmic scale on the vertical axis.

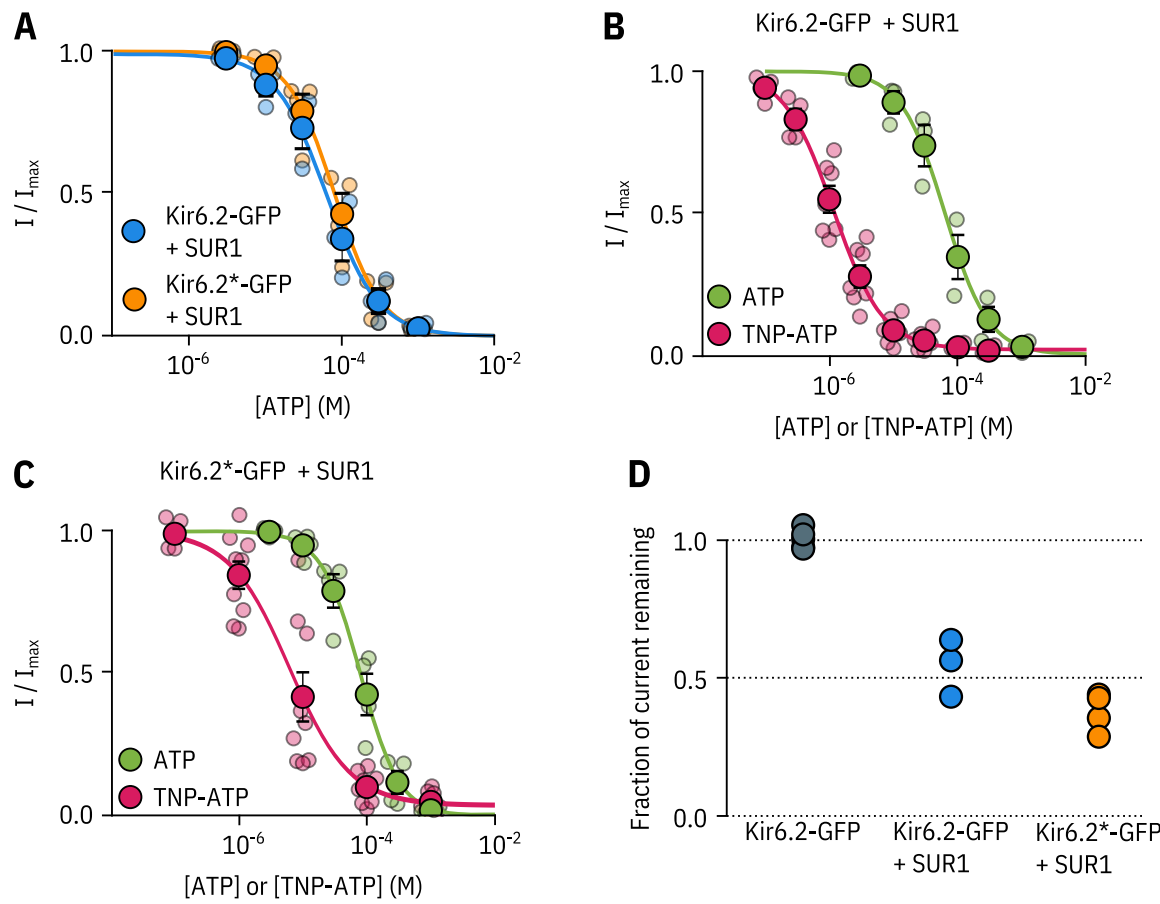


Figure 1 – figure supplement 2. Kir6.2*-GFP is functionally similar to Kir6.2-GFP. A. Concentration-response curve for ATP inhibition of Kir6.2-GFP + SUR1 or Kir6.2*-GFP + SUR1, measured in excised, inside-out patches. The smooth curves are descriptive Hill fits to the data. Kir6.2-GFP + SUR1: $IC_{50} = 62.7 \mu\text{M}$, $h = 1.28$, $I_{max} = 0.99$, $n = 3$; Kir6.2*-GFP + SUR1: $IC_{50} = 79.5 \mu\text{M}$, $h = 1.42$, $I_{max} = 1.00$, $n = 4$. **B, C.** Concentration-response relationships for current inhibition in excised, inside-out patches expressing Kir6.2-GFP + SUR1 (**C**) or Kir6.2*-GFP + SUR1 (**D**) exposed to either ATP or TNP-ATP. The smooth curves are descriptive Hill fits to the data. Kir6.2-GFP + SUR1 (TNP-ATP): $IC_{50} = 1.17 \mu\text{M}$, $h = 1.14$, $I_{max} = 0.97$, $n = 7$, Kir6.2*-GFP + SUR1 (TNP-ATP): $IC_{50} = 6.23 \mu\text{M}$, $h = 0.92$, $I_{max} = 0.96$, $n = 9$. Data and fits for inhibition of Kir6.2*-GFP + SUR1 by TNP-ATP are the same as in Figure 2. **D.** Fractional current inhibition by 100 μM tolbutamide measured in excised, inside out patches. Data were normalised to the average current in control solution before and after tolbutamide exposure. Each data point represents an individual patch. Kir6.2-GFP without SUR1, $n = 5$; Kir6.2-GFP + SUR1, $n = 3$; Kir6.2*-GFP + SUR1, $n = 4$.

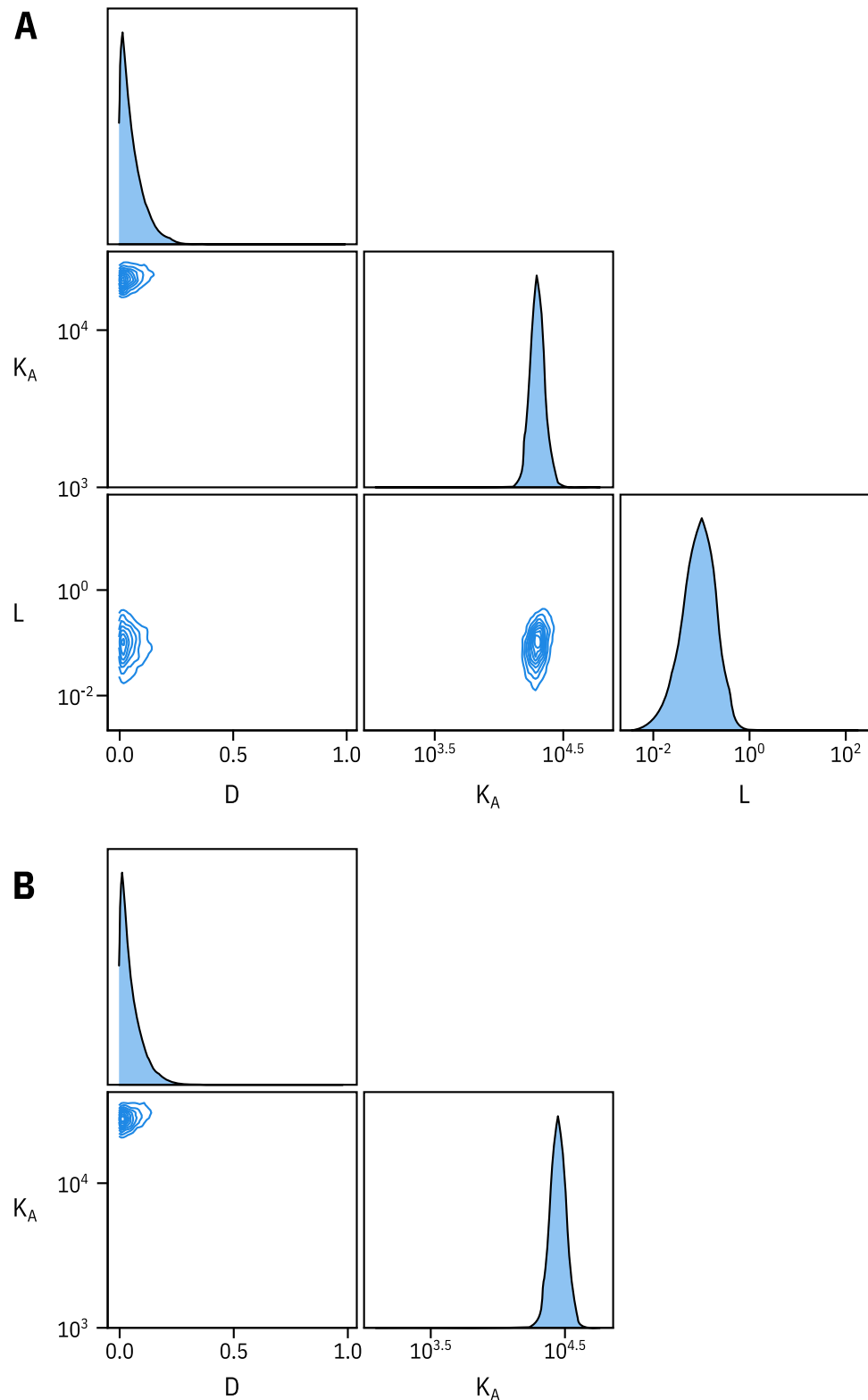


Figure 2 – figure supplement 1. Fixing L does not affect estimates of D and K_A . **A.** Pairwise correlation plots of L , D and K_A from the full MWC-type model fit to Kir6.2*-GFP + SUR1. **B.** Pairwise correlation plots of D and K_A from the full MWC-type model with L fixed to 0.8 ($P_{open} = 0.45$).

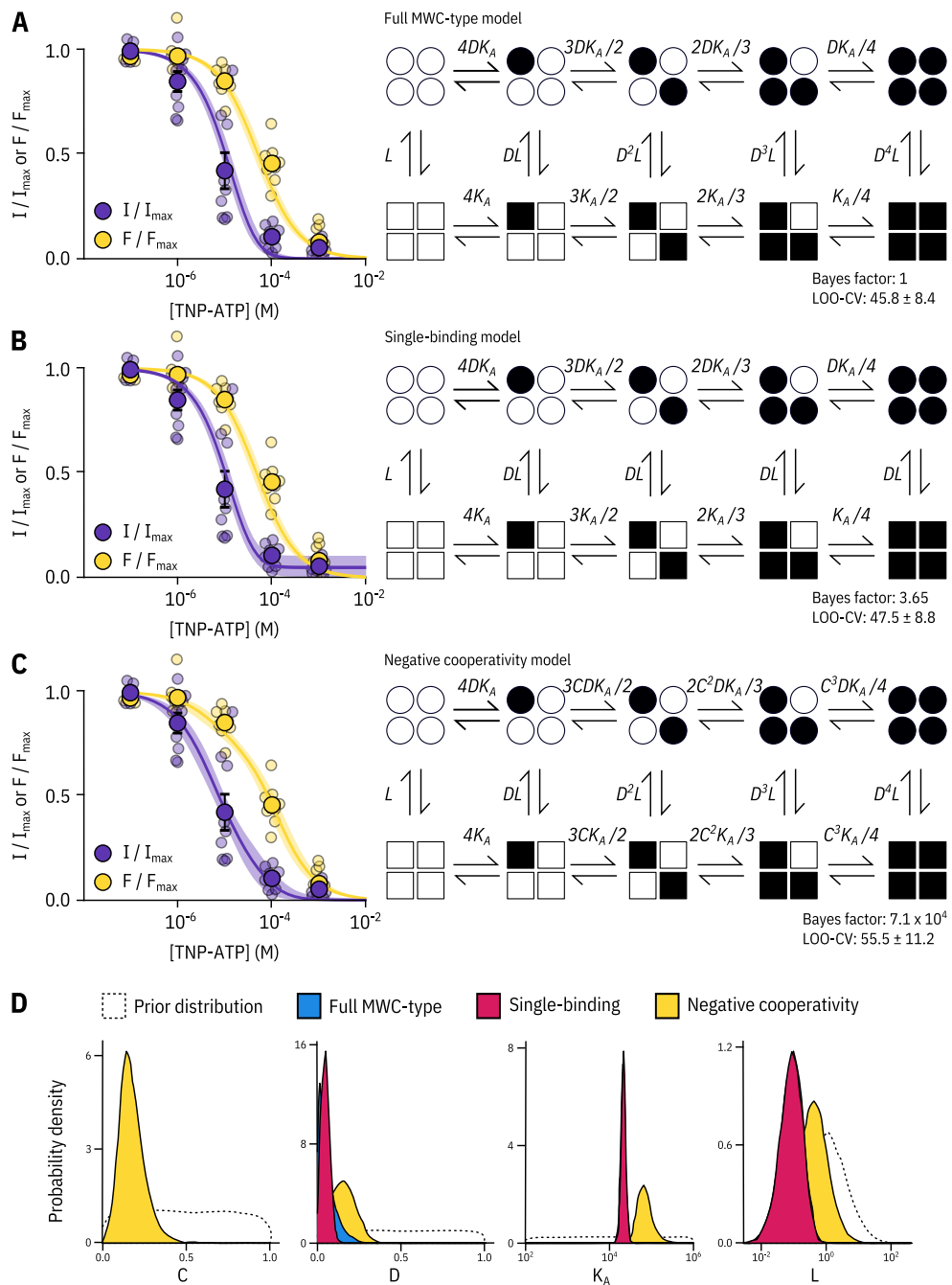


Figure 2 – figure supplement 2. Model selection. Fits to PCF data from Figure 2 with the full MWC-type model (**A**), single-binding model (**B**) and negative-cooperativity model (**C**) are shown on the left with the diagrammatic formulation of each model on the right. The Bayes factor and leave-one-out cross-validation (LOO-CV) scores for each model compared to the full MWC-type model are displayed. More detail on these fit indices is provided in the Discussion section. L , D , C , and K_A are defined in the text. **D**. Posterior probability distributions for the each of the models generated by MCMC fits to the data in Figure 2 overlaid on the prior probability distribution (dashed line) for each parameter. For L and K_A , the distributions for the MWC-type and single-binding model were virtually identical. The MWC-type densities are hidden behind the single-binding densities.

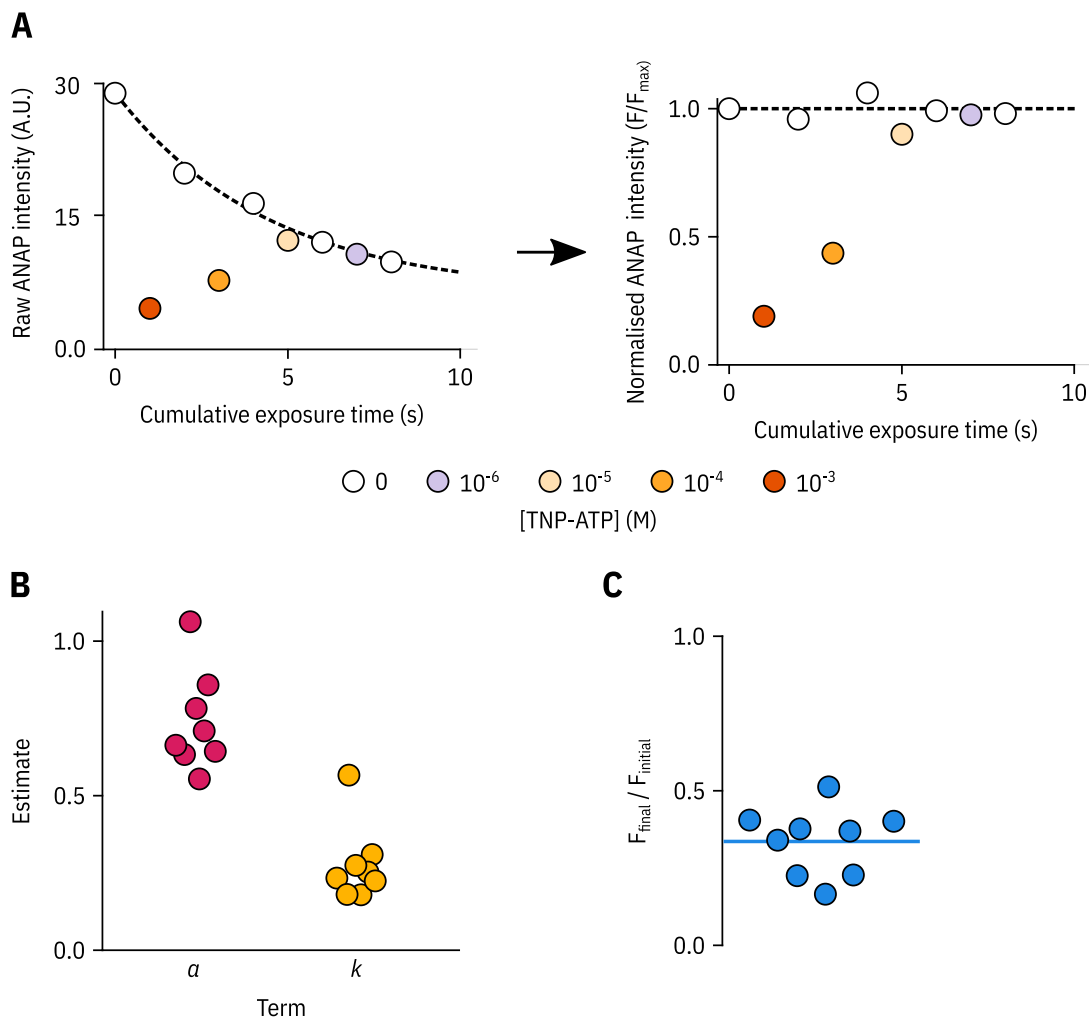


Figure 2 – figure supplement 3. Bleaching correction for PCF experiments. **A.** Raw ANAP fluorescence intensities (left) and corrected ANAP fluorescence intensities (right) from a representative PCF experiment with Kir6.2*-GFP + SUR1 plotted against the exposure time. The fit to Equation 1 is shown as a black dashed line. To minimise artifacts from our bleaching corrections we performed experiments from both high-to-low and low-to-high TNP-ATP concentrations. **B.** The parameters from fits to Equation 1 for each PCF experiment in Figure 2 are shown individually. **C.** The fraction of ANAP fluorescence intensity remaining at the end of each PCF experiment in Figure 2 is shown by dividing the raw ANAP intensity of the last exposure by that of the first. The mean fractional remaining intensity of 0.34 is shown as a horizontal blue line.

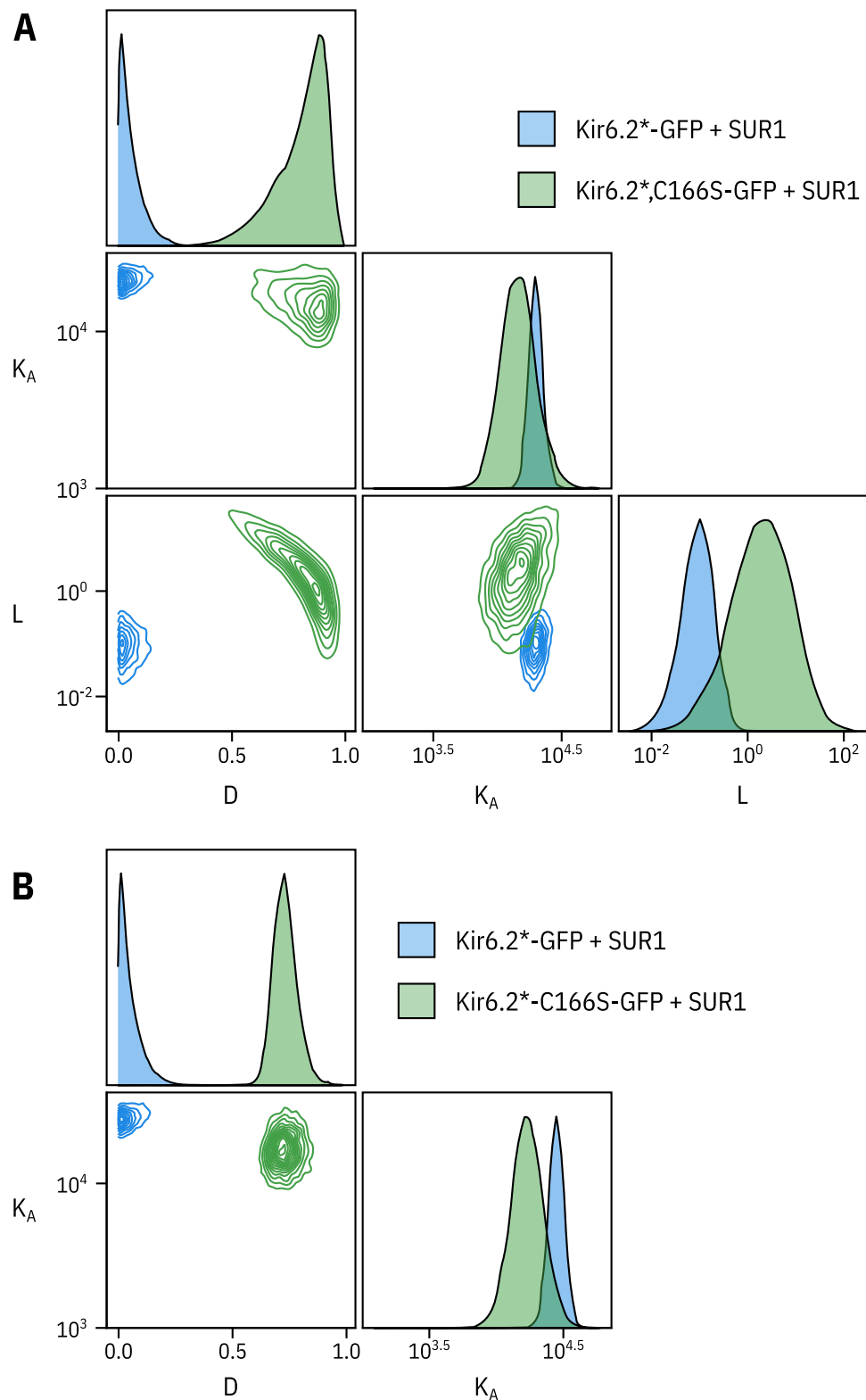


Figure 3 – figure supplement 1. Fixing L does not affect the other two parameters. **A.** Pairwise correlation plots of L , D and K_A from the full MWC-type model fit to $\text{Kir6.2}^*-\text{GFP} + \text{SUR1}$ and $\text{Kir6.2}^*,\text{C166S}-\text{GFP} + \text{SUR1}$. **B.** Pairwise correlation plots of D and K_A from the full MWC-type with L fixed to 0.8 for $\text{Kir6.2}^*-\text{GFP} + \text{SUR1}$ ($P_{open} = 0.45$) or 6.0 for $\text{Kir6.2}^*,\text{C166S}-\text{GFP} + \text{SUR1}$ ($P_{open} = 0.86$).

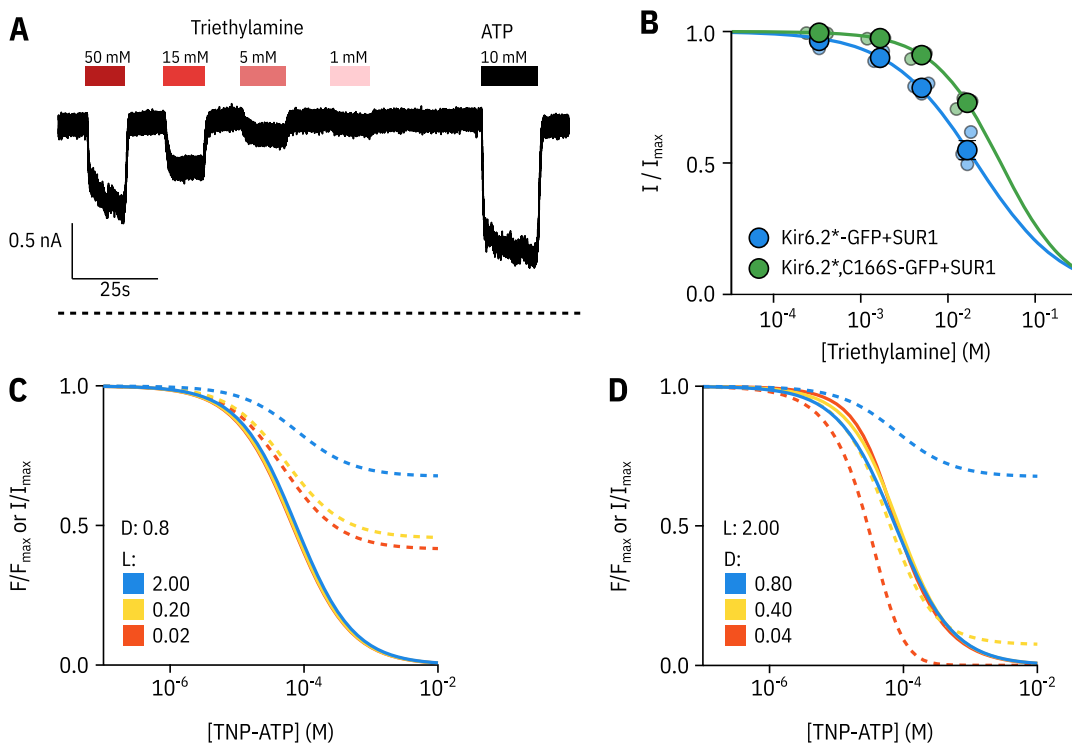


Figure 3 – figure supplement 2. AN MWC-type model predicts a nucleotide-insensitive current plateau for Kir6.2-C166S.

A. Representative current trace from an excised patch expressing Kir6.2*,C166S-GFP+SUR1 exposed to triethylamine (shown as shades of red) and 10 mM ATP (shown in black). **B.** Concentration dependence of triethylamine inhibition for Kir6.2*-GFP+SUR1 (blue data points) or Kir6.2*,C166S-GFP+SUR1 (green data points) in excised patches. The solid curves are descriptive Hill fits to the data with $1 - I_{max}$ set to 0. Kir6.2*-GFP + SUR1: $IC_{50} = 63.1$ mM, $h = 0.87$, $n = 3$, Kir6.2*,C166S-GFP + SUR1: $IC_{50} = 120$ mM, $h = 1.12$, $n = 3$. **C,D.** Predictions of our full MWC-type model for a range of values of L (**C**) or D (**D**). Fluorescence quenching (F/F_{max}) is shown as solid curves and current inhibition (I/I_{max}) is shown as dashed curves. The blue curves represent values taken from the fit to Kir6.2*,C166S-GFP+SUR1 shown in Figure 3D rounded to the nearest significant figure. Notably, the model predicts that if nucleotide inhibition is shifted to the right of nucleotide binding, we should expect to see a current plateau proportional to the unliganded open probability of the channel.

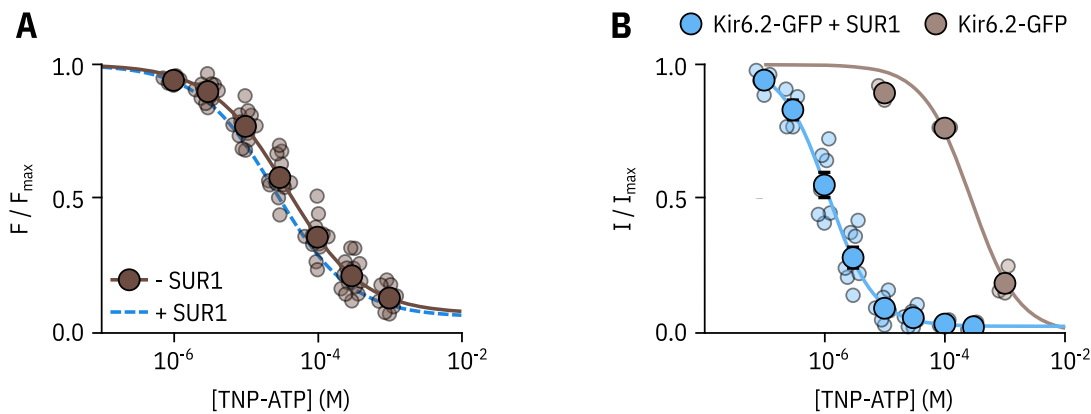


Figure 4 – figure supplement 1. SUR1 affects the apparent affinity for nucleotide binding to Kir6.2. **A.** Concentration dependence of TNP-ATP binding to unroofed membrane fragments expressing Kir6.2*-GFP without SUR1 (brown), expressed as quenching of ANAP fluorescence. The smooth curve is a descriptive Hill fit. Kir6.2*-GFP (no SUR1): $EC_{50} = 37.6 \mu\text{M}$, $h = 0.83$, $E_{max} = 0.92$, $n = 14$. The Hill fit to Kir6.2*-GFP + SUR1 is shown as a blue dashed curve. **B.** Concentration-response curve for TNP-ATP inhibition of Kir6.2-GFP (no ANAP label) without or with co-expression of SUR1, measured in excised, inside-out patches. Kir6.2-GFP + SUR1: $EC_{50} = 1.17 \mu\text{M}$, $h = 1.14$, $E_{max} = 0.97$, $n = 7$; Kir6.2-GFP (no SUR1): $EC_{50} = 273 \mu\text{M}$, $h = 1.09$, $E_{max} = 1.00$, $n = 3$.

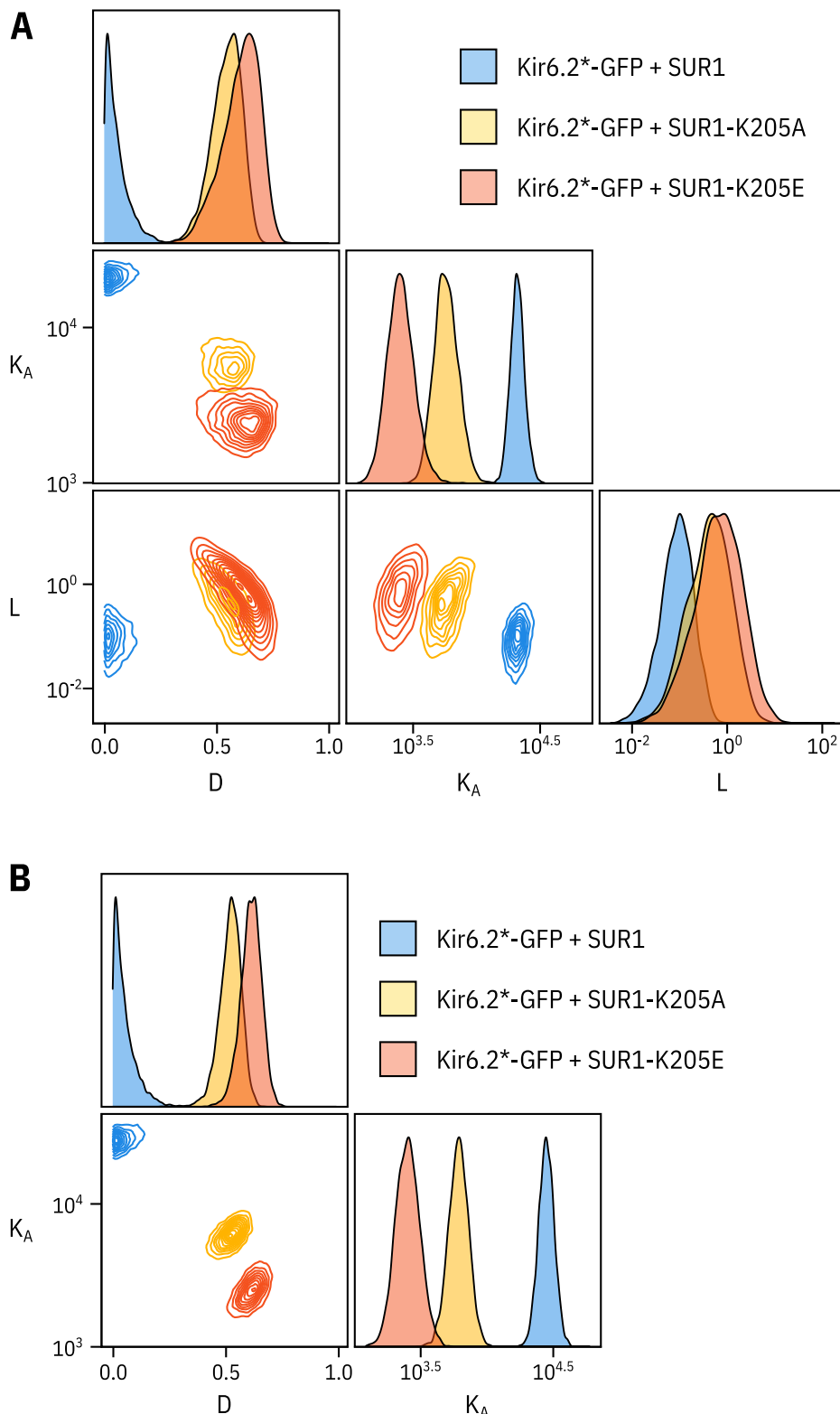


Figure 4 – figure supplement 2. Fixing the L parameter does not drastically affect the fits to the SUR1-K205A or

SUR1-K205E data. A. Pairwise correlation plots of L , D and K_A from the full MWC-type model fit to Kir6.2*-GFP co-expressed with wild-type SUR1, SUR1-K205A, and SUR1-K205E. **B.** Pairwise correlation plots of D and K_A from the full MWC-type as above with L fixed to 0.8 (*Trapp et al., 1998*).

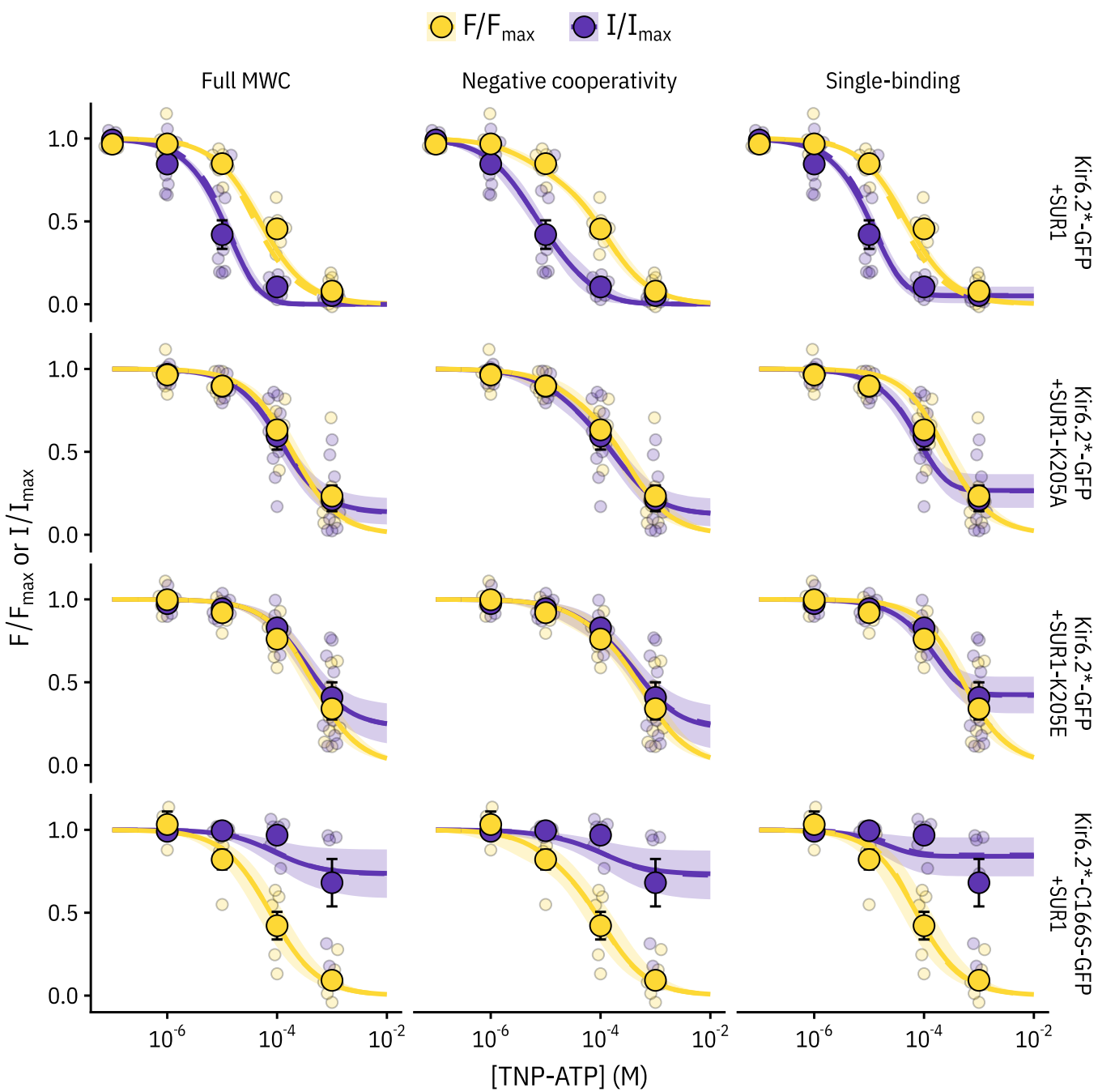


Figure 4 – figure supplement 3. Comparing the ability of each model to explain the data. Fits for each construct with each model (MWC-type, single-binding, negative-cooperativity) are displayed with the solid curve representing the median fit, the shaded area representing the 95% quartiles, and the dashed curve representing the median fit if the L parameter is fixed (to 6.0 for Kir6.2*,C166S-GFP + SUR1 and to 0.8 for the other three constructs). As the two fits were very similar, the dashed curve mostly overlays the solid curve. The most notable differences between the fits are that the negative cooperativity model allows for non-sigmoidal curves, and the single-binding model predicts much larger pedestals of current at saturating concentrations of TNP-ATP than either of the other two models.

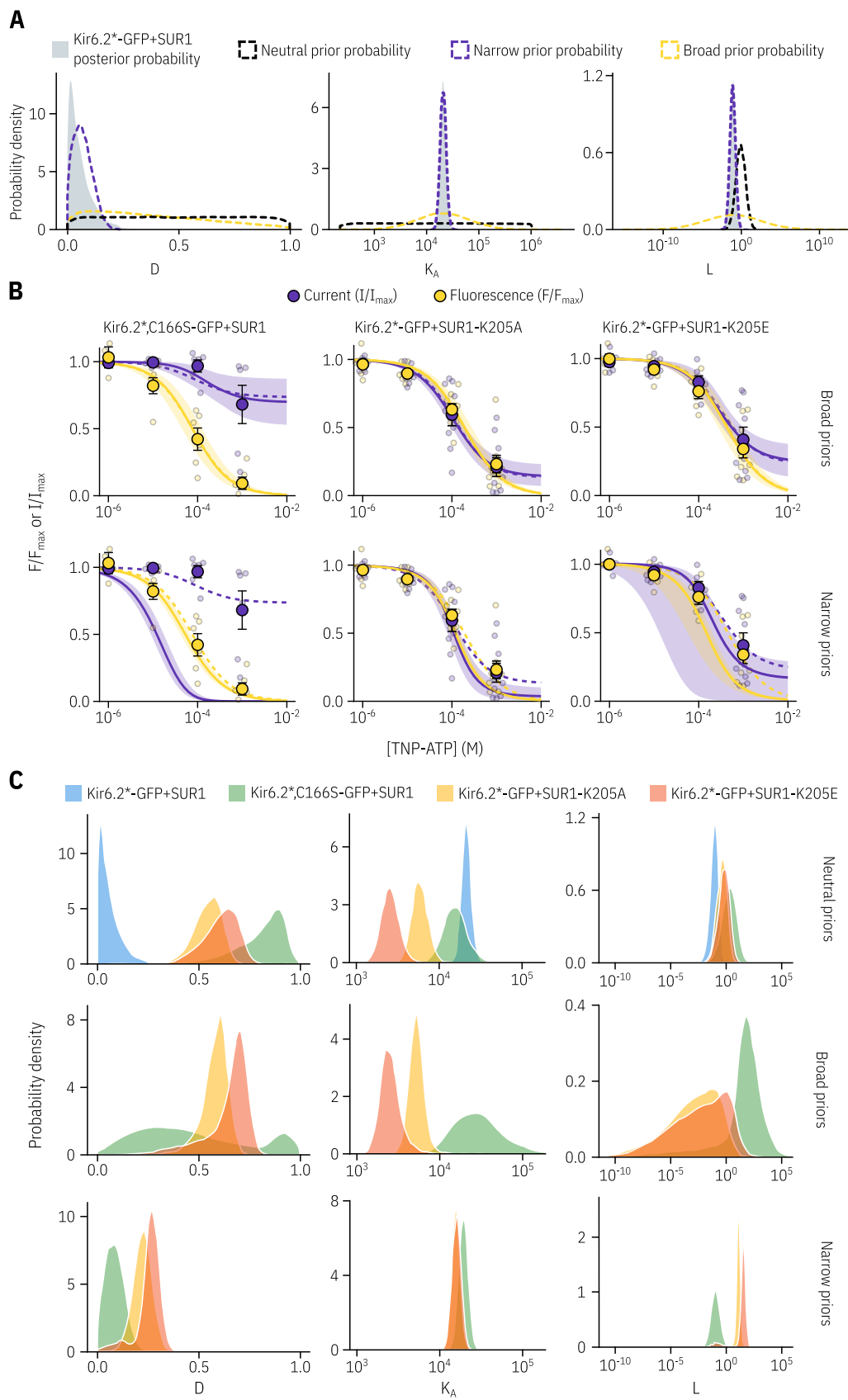


Figure 4 – figure supplement 4. A neutral choice of priors allows for the best fits to the data.

Figure 4 – figure supplement 4. A neutral choice of priors allows for the best fits to the data. **A.** We generated more informative priors (dashed lines) based on our posterior probability distributions for Kir6.2*-GFP + SUR1 (in grey) by fitting the posterior distribution for each parameter with a normal distribution. In addition to this narrow informative prior, we generated a broad informative prior still centered on the Kir6.2*-GFP + SUR1 posterior probability density by increasing the standard deviation of the fitted normal distribution by a factor of ten. **B.** Fits to the PCF data for all constructs tested using either the neutral priors reported earlier (shown as dashed lines), or priors based on the fits to Kir6.2*-GFP+SUR with the solid curves representing the median fit and the shaded area representing the 95% quantiles. **C.** The posterior probability distributions corresponding to the fits shown in **B** are shown for each parameter.